A Regional multi-Air Pollutant Assimilation System (RAPAS v1.0) for emission estimates: system development and application

Shuzhuang Feng[1], Fei Jiang[1,2], Zheng Wu[3], Hengmao Wang[1,2], Wei He[1], Yang Shen[1], Lingyu Zhang[1], Yanhua Zheng[1], Chenxi Lou[1], Ziqiang Jiang[4], Weimin Ju[1,2]

[1] *Jiangsu Provincial Key Laboratory of Geographic Information Science and Technology, International Institute for Earth System Science, Nanjing University, Nanjing, 210023, China*

[2] *Jiangsu Center for Collaborative Innovation in Geographical Information Resource Development and Application, Nanjing, 210023, China*

[3] *Chongqing Institute of Meteorological Sciences, Chongqing, 401147, China*

[4] *Jiangsu Environmental Monitoring Center, Nanjing, 210019, China*

Correspondence to: Fei Jiang (jiangf@nju.edu.cn)

Abstract

Top-down atmospheric inversion infers surface-atmosphere fluxes from spatially distributed observations of atmospheric compositions, which is a vital means for quantifying large-scale anthropogenic and natural emissions. In this study, we developed a Regional multi-Air Pollutant Assimilation System (RAPAS v1.0) based on the Weather Research and Forecasting/Community Multiscale Air Quality Modeling System (WRF/CMAQ) model, the three-dimensional variational (3DVAR) algorithm and the ensemble square root filter (EnSRF) algorithm. It is capable of simultaneously assimilating spatially distributed hourly in-situ measurements of CO, SO_2, NO_2, $PM_{2.5}$ and PM_{10} concentrations to quantitatively optimize gridded emissions of CO, SO_2, NO_x, primary $PM_{2.5}$ ($PPM_{2.5}$) and coarse PM_{10} (PMC) on regional scale. RAPAS includes two subsystems, initial field assimilation (IA) subsystem and emission inversion (EI) subsystem, which are used to generate a good chemical initial condition (IC), and conduct inversions of anthropogenic emissions, respectively. A "two-step" inversion scheme is adopted in the EI subsystem in each data assimilation (DA) window, in which the emission is inferred in the first step, and then, it is input into the CMAQ model to simulate the initial field of the next window, meanwhile, it is also transferred to the next window as the prior emission. The chemical IC is optimized through the IA subsystem, and the original emission inventory is only used in the first DA window. Besides, a "super-observation" approach is implemented based on optimal estimation theory to decrease the computational costs and observation error correlations and reduce the influence of representativeness errors.

With this system, we estimated the emissions of CO, SO_2, NO_x, $PPM_{2.5}$ and PMC in December and July 2016 over China using the corresponding nationwide surface observations. The 2016 Multi-resolution Emission Inventory for China (MEIC 2016) was used as the prior emission. For December, the system was run from 26 November to 31 December, in which the IA subsystem was run in the first 5 days, and the EI subsystem was run in the following days. In July, the system was run in the same way. The evaluation and sensitivity testing of this system mainly focused on December.

Results showed that the simulated concentrations of CO, NO_2, SO_2, $PM_{2.5}$ and PM_{10} with the prior inventory have large systematic biases, with relative biases in the range of -48.2-54.2%. In the IA subsystem, after 3DVAR, the root mean squared error (RMSE) of the simulated concentrations decreased by 50.0-73.2%, and the correlation coefficient (CORR) increased to 0.78-0.92 for the five species. In the EI subsystem, after emission inversions, the RMSE of the simulated concentrations decreased by 40.1-56.3%, and the CORR increased to 0.69-0.87. For the whole mainland China, the uncertainties were reduced by 44.4%, 45.0%, 34.3%, 51.8% and 56.1% for CO, SO_2, NO_x, $PPM_{2.5}$ and PMC, respectively. Overall, compared to the prior emission (MEIC 2016), the posterior emissions increased by 129%, 20%, 5%, and 95% for CO, SO_2, NO_x and $PPM_{2.5}$, respectively, indicating that there was significant underestimation in the MEIC inventory. The posterior PMC emissions, including anthropogenic and natural dust contributions, increased by 1045%. A series of sensitivity tests were conducted with different inversion processes, prior emissions, prior uncertainties, and observation errors. Results showed that the "two-step" scheme clearly outperformed the simultaneous assimilation of ICs and emissions ("one-step" scheme), and the system is rather robust in estimating the emissions using the nationwide surface observations over China. Our study offers a useful tool for accurately quantifying multi-species anthropogenic emissions at large scales and near-real time.

1. Introduction

Due to rapid economic developments and pollution control legislations, an increasing demand to provide updated emission estimates has arisen, especially in areas where anthropogenic emissions are intensive. Accurately estimating source emission quantities and spatiotemporal changes resulting from various regulations is imperative and valuable for understanding air quality responses and crucial for providing timely instructions for the design of future emissions regulations. However, most inventories have been developed based on a bottom-up approach and are usually updated with a few years delay due to the complexity of gathering all statistical information on activity levels and sector-specific emission factors (Ding et al., 2015). The large uncertainty associated with the low temporal and spatial resolution of these datasets also greatly limits the assessment of emission changes. Some studies (Bauwens et al., 2020; Shi and Brasseur, 2020) have evaluated emission changes indirectly through concentration measurements, but air pollution changes are not only dominated by emission changes, but also highly affected by meteorological conditions (Shen et al., 2021).

Top-down atmospheric inversion infers surface-atmosphere fluxes from spatially distributed observations of atmospheric compositions. Recent efforts have focused on developing air pollution data assimilation (DA) system to conduct the top-down inversion, which is able to integrate model and multi-source and large amounts of observational information to constrain emission sources. Two major methods, namely, 4D-variational data assimilation (4DVAR) and ensemble Kalman filter (EnKF), are widely used in those DA systems. 4DVAR provides a global optimal analysis through minimizing a cost function. It shows implicit flow-dependent background error covariance and can reflect complex nonlinear constraint relationship (Lorenc, 2003). Additionally, the model error can be partly accounted for with a weak constraint 4DVAR method through the definition of a systematic error term in a cost function (Derber, 1989). For example, GEOS-Chem and TM5 4DVAR frameworks have been used to estimate CH_4 (Alexe et al., 2015; Schneising et al., 2009; Stanevich et al., 2021; Wecht et al., 2014) and CO_2 fluxes (Basu et al., 2013; Nassar et al., 2011; Wang et al.,

2019a) from different satellite retrieval products. Monteil et al. (2013) showed that the global patterns of CH_4 emissions derived from SCIAMACHY (with bias correction) and GOSAT retrievals are in remarkable agreement based on 15 months observations. Additionally, Jiang et al. (2017) used 4DVAR algorithm to estimate global CO emission trends from 2000–2015 using MOPITT retrievals. Kurokawa et al. (2009) and Stavrakou et al. (2008) also used 4DVAR technique to estimate NO_x emission changes. However, the drawback of the 4DVAR method is the additional development of adjoint models that are technically difficult and cumbersome for complex chemical transport models. Instead, EnKF uses the flow-dependent background error covariance generated by ensemble simulations to map the deviations in concentrations to increments of emissions, which is more flexible and easier to implement. Many previous studies have used EnKF techniques to assimilate the single or dual species observations to optmize the corresponding emission species (Chen et al., 2019; Peng et al., 2017; Schwartz et al., 2014; Sekiyama et al., 2010). Multispecies data assimilation has shown the advantage of efficiently reducing the uncertainty in emission inventories and has led to improvements in air quality forecasting (Ma et al., 2019; Miyazaki et al., 2012b), since it would offer additional constraints on emission estimates through the improvements in related atmospheric fields, chemical reactions, and gas-particle transformations (Miyazaki and Eskes, 2013). Barbu et al. (2009) updated sulfur oxide (SO_x) emissions with SO_2 and sulfate aerosol observations and found that simultaneous assimilation of both species had better performance than assimilating one of them alone.

The deviation in chemical initial condition (IC) is one of the important sources of error that affects the accuracy of emission inversion, because atmospheric inversion fully attributes the biases in simulated and observed concentrations to the deviations in emissions (Meirink et al., 2006; Peylin et al., 2005). The biases of concentrations would be compensated through unreasonable adjustment of pollution emissions without the optimization of ICs (Tang et al., 2013). Tang et al. (2011) reported that the simultaneous optimizations of the ICs of O_3, NO_x and volatile organic compounds (VOCs) and the emissions of NO_x and VOCs produced an overall better performance in ozone forecasts

than the adjustment in emissions only. Similar method of simultaneously optimizing chemical ICs and emissions were also applied to constraining emissions in many previous studies (Ma et al., 2019; Miyazaki et al., 2012a; Peng et al., 2018). Although a large improvement has been achieved, this method still has great limitations because the contributions from the emissions and the chemical ICs to the model's bias are difficult to distinguish (Jiang et al., 2017). In addition, in this method, the constraints of the chemical ICs with observations in each assimilation window make the emission inversions are independent between assimilation windows, means if the emission in one window is overestimated or underestimated, it cannot be transferred to the next window for further correcting and be compensated in the following windows. This may result in a systematic bias in the inverted emissions (Jiang et al., 2021).

Since 2013, China has deployed an air pollution monitoring network that publishes nationwide and real-time hourly surface atmospheric observations. This dataset provides an opportunity to improve emission estimates using DA. In this study, a regional multi- air pollutant assimilation system introducing 3DVAR and EnKF DA techniques is constructed to simultaneously assimilate various surface observations (e.g., CO, SO_2, NO_2, O_3, $PM_{2.5}$ and PM_{10}). Considering the possible shortcomings of the simultaneous optimization method (named as "one-step" method in this study) as metioned by Jiang et al. (2021), we adopted a "two-step" method (Sect. 3) in this system. Unlike the "one-step" method, the ICs of each DA window in the "two-step" method is simulated using the posterior emissions of the pervious DA window. The capability of RAPAS in reanalysis field generation and emission inversion estimation was evaluated. The robustness of the system was also investigated with different prior inventories, uncertainty settings of the prior emission, and observation errors. This paper is organized as follows: in Sect. 2, we introduce the DA system and the observation data, and in Sect. 3, we describe the experimental design. The results of the system performance and sensitivity tests are presented and discussed in Sect. 4, followed by the conclusions in Sect. 5.

2. Method and data

2.1 System description

2.1.1 Procedure of the assimilation system

A regional air pollutant assimilation system has been preliminarily constructed and successfully applied in our previous studies to optimize gridded CO and NO_x emissions (Feng et al., 2020a; Feng et al., 2020b). Herein, the system was further extended to simultaneously assimilate multiple species (e.g., CO, SO_2, NO_2, O_3, $PM_{2.5}$ and PM_{10}) and officially named as the Regional multi- Air Pollutant Assimilation System (RAPASv1.0). The RAPAS mainly includes three components: a regional chemical transport model (CTM), which is coupled offline and used to simulate the meteorological fields and atmospheric compositions, and the 3DVAR and ensemble square root filter (EnSRF) modules, which are used to optimize chemical ICs (Feng et al., 2018; Jiang et al., 2013b) and anthropogenic emissions (Feng et al., 2020a; Feng et al., 2020b), respectively. The introduction of 3DVAR mainly considers its great performance based on our previous study and lower computational cost during spin-up period in optimizing ICs. Additionally, it has been found that the 3DVAR method can obtain a better initial field than the EnKF method (Schwartz et al., 2014).

Based on above three components, the RAPAS is divided into two subsystems, namely the IC assimilation (IA) subsystem (CTM plus 3DVAR) and the emission inversion (EI) subsystem (CTM plus EnSRF). As shown in Figure 1, the IA subsystem is first run to optimize chemical ICs (Kleist et al., 2009; Wu et al., 2002) for the subsequent EI subsystem. In the IA subsystem, we do not need to distinguish the type of sources of the model-observation mismatch error. The EI subsystem runs cyclically with a "two-step" scheme. In the first step, the prior emissions (X^b) are perturbed and put into the CTM model to simulate chemical concentration ensembles. The simulated concentrations of the lowest model level are then interpolated to the observation space according to the locations and times of the observations using the nearest neighbor interpolation method. The prior emissions (X^b), simulated observations and real

observations are entered into the EnSRF module to generate the optimized emissions (X^a). In the second step, the optimized emissions are entered into the CTM model again to generate the initial fields of the next DA window. Meanwhile, the optimized emissions are transferred to the next window as the prior emissions. Different from the "one-step" scheme, this "two-step" scheme needs to run the CTM model twice, which is time consuming, but it could transfer the potential errors of the inverted emissions in one DA window to the next for further correction. The benefit of this scheme will be further presented in Sect. 4.3.
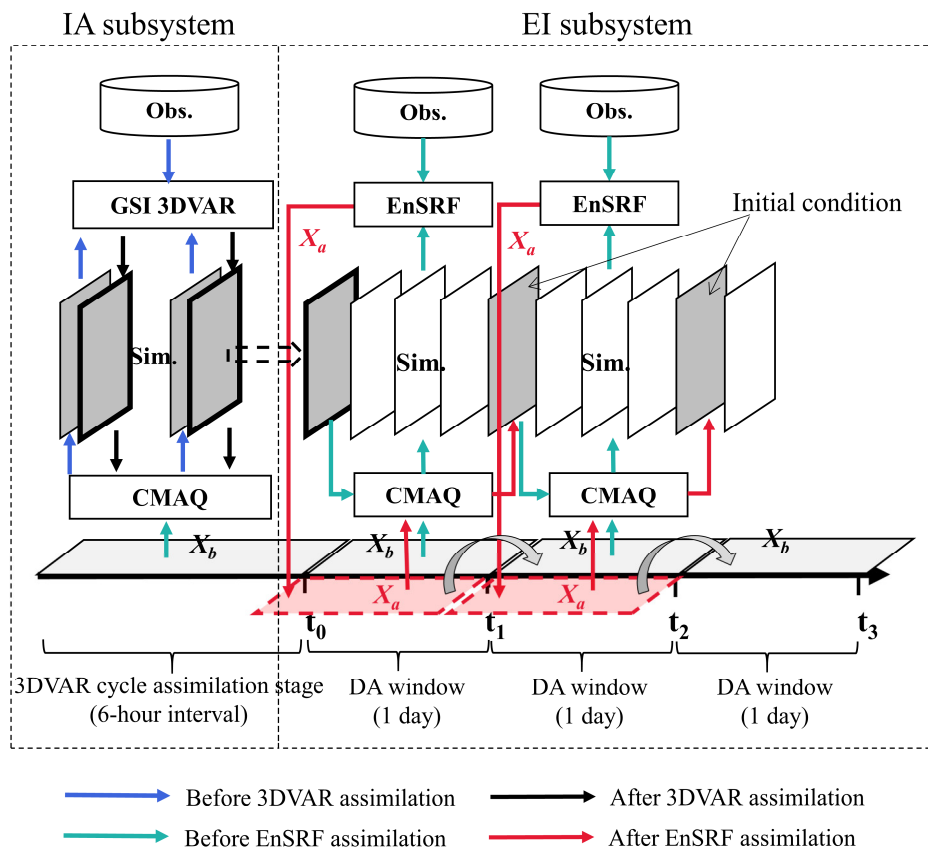
Figure 1. The composition and flow chart of RAPAS. The $\mathbf{x_a}$ and $\mathbf{x_b}$ represent the prior and posterior emissions. The 3DVAR assimilation stage lasts 5 days with data input frequency of 6 hours, and the DA window in the EI subsystem is set to 1 day.

2.1.2 Atmospheric transport model

The regional chemical transport model of WRF/CMAQ was adopted in this study. CMAQ is a regional 3-D Eulerian atmospheric chemistry and transport model with a

"one-atmosphere" design developed in the US Environmental Protection Agency (EPA). It can address the complex interactions among multiple pollutants/air quality issues simultaneously. CMAQ was driven by the WRF model, which is a state of the art mesoscale numerical weather prediction system designed for both atmospheric research and meteorological field forecasting. In this study, WRF version 4.0 and CMAQ version 5.0.2 were adopted. The WRF simulations were performed with a 36-km horizontal resolution on 169×129 grids, and it covers the whole of mainland of China (Figure 2). This spatial resolution has been widely adopted in regional simulations and can provide good simulations of the spatiotemporal variations of air pollutants (Mueller and Mallard, 2011; Sharma et al. 2016). In the vertical direction, there are 51 sigma levels on sigma-pressure coordinates extending from the surface to 100 hPa. The underlying surface of urban and built-up land was replaced by the MODIS land cover retrieval of 2016 to adapt to the rapid expansion of urbanization. The CMAQ model is run with the same domain but with three grid cells removed from each side of the WRF domain. There are 15 layers in the CMAQ vertical coordinate, which were interpolated from the 51 WRF layers.

The meteorological initial and lateral boundary conditions are both provided by the Final (FNL) Operational Global Analysis data of the National Center for Environmental Prediction (NCEP) with a $1° \times 1°$ resolution at 6-h intervals. The chemical lateral boundary conditions and chemical ICs in the IA subsystem come from the background profiles. As mentioned above, in the EI subsystem, the chemical IC in the first window is provided by the IA subsystem, and in the following windows, it is forward simulated using optimized emission from the previous window. The Carbon Bond 05 with updated toluene chemistry (CB05tucl) and the 6th generation aerosol module (AERO6) are chosen as the gas-phase and aerosol chemical mechanisms, respectively (Appel et al., 2013; Sarwar et al., 2012). Detailed physical and chemical configurations are listed in Table 1.
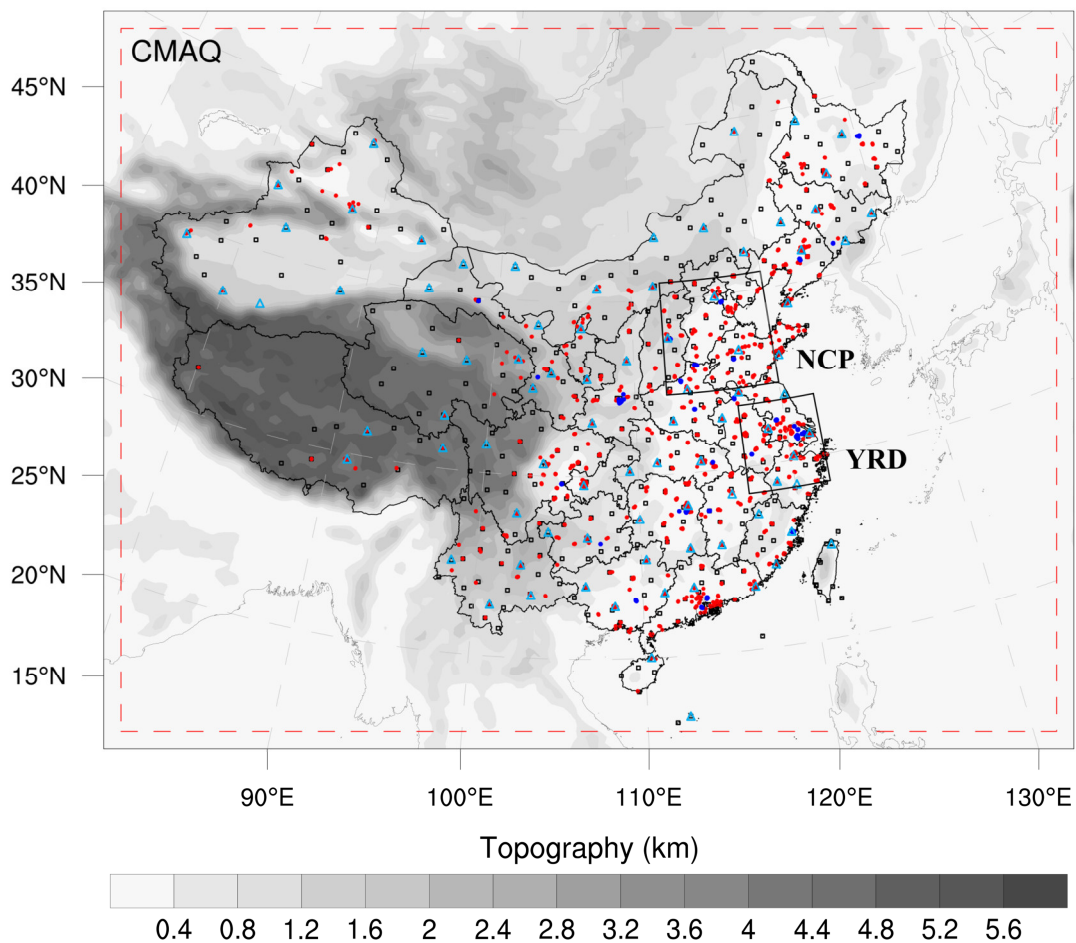
Figure 2. Model domain and observation network. The red dashed frame depicts the CMAQ computational domain; the black squares represent the surface meteorological measurement sites; the turquoise triangles represent the sounding sites; and the red and blue dots represent the air pollution measurement sites. Observations of all sites are assimilated in the 3DVAR subsystem, while observations of city sites where red dots are averaged are used for assimilation and where green dots are averaged are used for independent evaluation in EI subsystem; the boxed subregions are the North China Plain (NCP) and Yangtze River Delta (YRD); and the shaded area depicts the topography.

256   **Table 1**. Configuration options of WRF/CMAQ

WRF		CMAQ	
Parameter	Scheme	Parameter	Scheme
Microphysics	WSM6	Horizontal/Vertical advection	yamo/wrf
Longwave	RRTM	Horizontal/Vertical diffusion	multiscale/acm2
Shortwave	Goddard	Deposition	m3dry
Boundary layer	ACM	Chemistry solver	EBI
Cumulus	Kain-Fritsch	Photolysis	phot_inline
Land-surface	Noah	Aerosol module	AERO6
Surface layer	Revised	Cloud module	cloud_acm_ae6
Urban canopy	No	Gas-phase chemistry	CB05tucl

257   **2.1.3 3DVAR assimilation algorithm**

258   The Grid-point Statistical Interpolation (GSI) developed in the US National Centers for

259   Environmental Prediction (NCEP) was employed in this study. Building upon the work

260   of Liu et al. (2011), Jiang et al. (2013b) and Feng et al. (2018), we extended it to

261   simultaneously assimilate multiple species (including CO, SO_2, NO_2, O_3, $PM_{2.5}$, and

262   PM_{10}) and first used individual aerosol species of $PM_{2.5}$ as analysis variables within the

263   GSI/WRF/CMAQ framework. Additional work includes the construction of surface air

264   pollutant observation operators, the updating of observation errors, and the statistics of

265   background error covariance for the analysis variables. Moreover, the data interface

266   was also modified to read/write the CMAQ output/input file directly, which is easy to

267   implement.

268   In the sense of a minimum analysis error variance, the 3DVAR algorithm optimizes

269   analysis fields with observations by iterative processes to minimize the cost function

270   (J(x)) defined below:

271    $J(x) = \frac{1}{2}(\mathbf{x_a} - \mathbf{x_b})^T \mathbf{B}^{-1}(\mathbf{x_a} - \mathbf{x_b}) + \frac{1}{2}[H(\mathbf{x_a}) - \mathbf{y}]^T \mathbf{R}^{-1}[H(\mathbf{x_a}) - \mathbf{y}],$ (1)

272 where $\mathbf{x_a}$ is a vector of the analysis field; $\mathbf{x_b}$ denotes the background field; $\mathbf{y}$ is the

273 vector of observations; $\mathbf{B}$ and $\mathbf{R}$ are the background and observation error covariance

274 matrices, respectively, representing the relative contributions to analysis; and H is the

275 observation operator that maps the model variables to the observation space.

276 The analysis variables are the 3D mass concentrations of the pollution compositions

277 (e.g., CO and sulfate) at each grid point. Hourly mean surface pollution observations

278 within a 1 hour window of the analysis are assimilated. To assimilate the surface

279 pollution observations, model-simulated compositions are first diagnosed at the

280 observation locations. For gas concentrations that are directly used as analysis variables,

281 data units need to be converted from ppm or ppb to mg m^{-3} or μg m^{-3} to match with

282 observations. The model-simulated PM$_{2.5}$ and PM$_{10}$ concentrations at the ground level

283 are diagnosed as follows:

284 $PM_{2.5} = f_i \times PM_i + f_j \times PM_j + f_k \times PM_k = \text{OC} + \text{EC} + SO_4^{2-} + NO_3^- + NH_4^+ +$

285 $SEAS + AP_{2.5}$ (2)

286 $PM_{10} = PM_i + PM_j + PM_k = PM_{2.5} + PMC$ (3)

287 where f_i, f_j, and f_k are the PM$_{2.5}$ fractions of the Aitken, accumulation, and coarse

288 modes, respectively. These ratios are recommended as the concentrations of PM$_{2.5}$ and

289 fine mode aerosols (i.e., Aitken plus accumulation) could differ because the PM$_{2.5}$

290 particles include small tails from the coarse mode in the CMAQ model (Binkowski and

291 Roselle, 2003; Jiang et al., 2006). PM_i, PM_j, and PM_k represent the mass

292 concentrations of the 3 modes in the CMAQ model. Seven aerosol species of PM$_{2.5}$,

293 including organic carbon (OC), elemental carbon (EC), sulfate (SO_4^{2-}), nitrate (NO_3^-),

294 ammonium (NH_4^+), sea salt (SEAS), and fine-mode unspeciated aerosols ($AP_{2.5}$), and

295 additional coarse PM$_{10}$ (PMC) are extracted as analysis variables, which are updated

296 by the PM$_{2.5}$ and PMC observations, respectively. Before the calculation of equation (1)

297 within the GSI, the analysis variables are bilinearly interpolated in the horizontal

298 direction to the observation locations.

299 The computation of background error covariance (**B**) is generally costly and difficult

300 when a high-dimensional numerical model is used. For simplification, **B** is represented

301 as a product of spatial correlation matrices and standard deviations (SDs):

302 $$\mathbf{B} = \mathbf{D}\boldsymbol{C}\boldsymbol{D}^T \tag{4}$$

303 $$\mathbf{C} = \boldsymbol{C}_x \otimes \boldsymbol{C}_y \otimes \boldsymbol{C}_z \tag{5}$$

304 where **D** is the background error SD matrix, **C** is the background error correlation

305 matrix, $\otimes$ denotes the Kronecker product, and $\boldsymbol{C}_x$, $\boldsymbol{C}_y$, and $\boldsymbol{C}_z$ denote three one-

306 dimensional correlation submatrices in the longitude, latitude, and vertical coordinate

307 directions, respectively. $\boldsymbol{C}_x$ and $\boldsymbol{C}_y$ are assumed to be isotropic horizontally such that

308 can be represented using a Gaussian function. The correlation between any two points

309 x_i and x_j in the horizontal can be expressed as follows:

310 $$c\left(x_i,\ x_j\right) = e^{-\frac{(x_i - x_j)^2}{2L^2}} \tag{6}$$

311 where L is the horizontal correlation scale, which is estimated using the proxy of the

312 background error (Figure 3). The vertical correlation matric $\boldsymbol{C}_z$ is directly estimated

313 from the model background field since $\boldsymbol{C}_z$ is only an $n_z \times n_z$ (here, n_z=15) matrix.

314
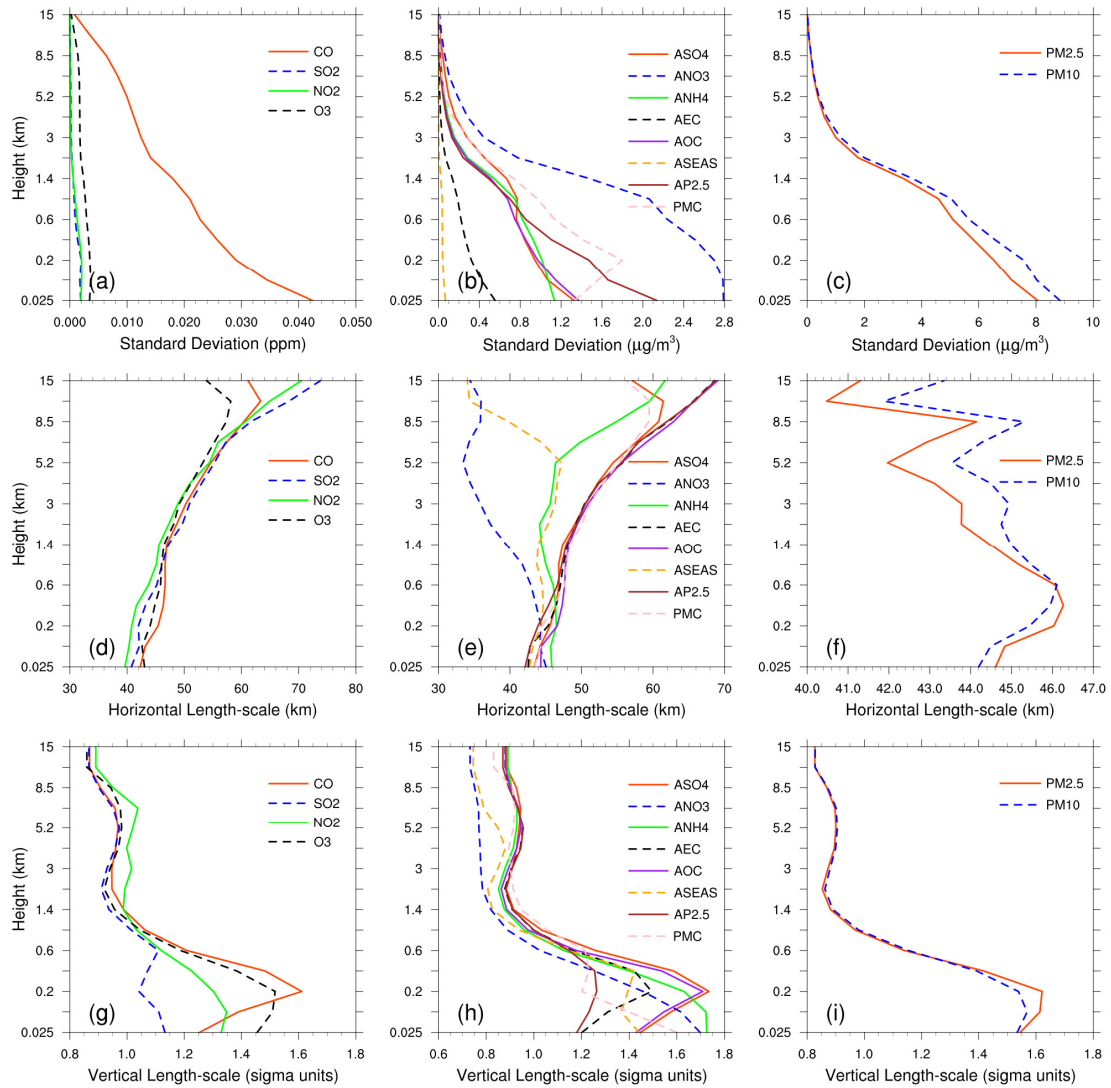
Figure 3. Vertical profiles of standard deviations (top, μg m⁻³), horizontal length scale (middle, km) and vertical length scale (bottom, km) for CO, SO₂, NO₂, O₃, sulfate, nitrate, ammonium, EC, OC, sea salt, unspeciated aerosols (AP2.5), PMC, PM₂.₅ and PM₁₀.

To estimate these matrices, the "NMC" method is used here to compute **B** for each variable by taking the differences between forecasts of different lengths valid at the same time (Parrish and Derber, 1992; Rabier et al., 1998). Differences between 24- and 12-h WRF/CMAQ forecasts of 60 pairs (two pairs a day) of analysis variables valid at either 0000 or 1200 UTC over November 2016 are used. The horizontal and vertical length scales of the correlation matrices are estimated by recursive filters (Purser et al., 2003). The vertical distribution of background error SDs is shown in Figure 3, which

326 varies with height and species. The vertical profile of the background error SDs

327 corresponds to the vertical concentration distribution. This means that higher

328 concentrations tend to have larger background error SDs (e.g., CO and nitrate). These

329 SDs exhibit a common reduction with height, especially at the top of the boundary layer.

330 The horizontal correlation of background error determines the propagation of

331 observation information in this direction, while vertical correlation determines the

332 vertical extension of such increments. For gaseous pollutants and most individual

333 aerosol components, the horizontal length scales increase with height, while for the total

334 particulate matter (i.e., $PM_{2.5}$ and PM_{10}), the scales increase with height in the boundary

335 layer and decrease with height in the free troposphere. The ground-level scale generally

336 spreads 40-45 km for all control variables on average. The vertical length scale of most

337 species increases first and then decreases with height, which may be related to the

338 vertical mixing (Kahnert, 2008) and stack emissions at about 200 m height.

339 **2.1.4 EnKF assimilation algorithm**

340 In EnKF, the time-dependent uncertainties of the state variables are estimated using a

341 Monte Carlo approach through an ensemble. Uncertainty can be propagated with linear

342 or nonlinear dynamic models (flow-dependent background error covariance) by simply

343 implementing ensemble simulations. The EnSRF algorithm introduced by Bierman

344 (1977) and Maybeck (1979) is used to constrain pollution emissions in this study.

345 EnSRF is a deterministic EnKF that obviates the need to perturb observations, which

346 has a higher computational efficiency and a better performance (Sun et al., 2009).

347 The perturbation of prior emissions represents the uncertainty. We implement additive

348 emission adjustment methods, which are calculated using the following function.

349 $$\boldsymbol{X}_i^b = \boldsymbol{X}_0^b + \boldsymbol{\delta X}_i^b, \text{i} = 1, 2, ..., \text{N} \tag{7}$$

350 where $\boldsymbol{b}$ represents the background (prior) state, i is the identifier of the perturbed

351 samples, N is the ensemble size, which was set to 40 in consideration of a tradeoff

352 between the computation cost and inversion accuracy (Figure S1), and $\boldsymbol{\delta X}_i^b$ represents

353 the randomly perturbed samples that are added to the prior emissions $\boldsymbol{X}_0^b$ to produce

ensemble samples of the inputs X_i^b. δX_i^b is drawn from Gaussian distributions with a mean of zero and the standard deviation of the prior emission uncertainty in each grid. The state variables of the emissions include CO, SO_2, NO_x, primary $PM_{2.5}$ ($PPM_{2.5}$) and PMC. We used variable localization to update the analysis, which means that the covariance among different state variables was not considered, and the emission of one species was only constrained with its corresponding air pollutant observation. This method has been widely used in chemical data assimilation systems to avoid spurious correlations among species. (Ma et al., 2019; Miyazaki et al., 2012b).

After obtaining an ensemble of state vectors (prior emissions), ensemble runs of the CMAQ model are conducted to propagate these errors in the model with each ensemble sample of state vectors. Combined with observational vector y, the state vector is updated by minimizing the analysis variance:

$$\overline{X^a} = \overline{X^b} + \mathbf{K}(\mathbf{y} - H\overline{X^b}) \tag{8}$$

$$\mathbf{K} = P^b H^T (H P^b H^T + R)^{-1} \tag{9}$$

$$P^b = \frac{1}{N-1} \sum_{i=1}^{N} (X_i^b - \overline{X}^b)(X_i^b - \overline{X}^b)^T \tag{10}$$

$$\delta X_i^a = \delta X_i^b - \widetilde{K} H \delta X_i^b \tag{11}$$

While employing sequential assimilation and independent observations, $\widetilde{K}$ is calculated as follows:

$$\widetilde{K} = \left(1 + \sqrt{R \big/ (H P^b H^T + R)}\right)^{-1} \mathbf{K} \tag{12}$$

where $\overline{X}^b$ represents the mean of the ensemble samples; H is the observation operator that maps simulated concentrations from model space to observation space; $y - H\overline{X^b}$ reflects the differences between the simulated and observed concentrations; P^b is the ensemble-estimated background (a priori) error covariance; $P^b H^T$ contains the response of the uncertainty in the simulated concentrations to the uncertainty in emissions; K is the Kalman gain matrix of the ensemble mean depending on the P^b

379 and observation error covariance $\boldsymbol{R}$, representing the relative contributions to analysis;

380 and $\widetilde{\boldsymbol{K}}$ is the Kalman gain matrix of the ensemble perturbation, which is used to

381 calculate emission perturbations after inversions $\delta\boldsymbol{X}_i^a$. The ensemble mean $\overline{\boldsymbol{X}^a}$ of the

382 analyzed state is taken as the best estimate of the emissions.

383 With large volumes of site observations that are recorded at a much higher resolution

384 than the model grid spacing, there would be significant correlated or fully consistent

385 model-data mismatch errors in one cluster, resulting in excessive adjustments and

386 deteriorated model performances (Houtekamer and Mitchell, 2001). To reduce the

387 horizontal observation error correlations and the influence of representativeness errors,

388 a "super-observation" approach combining multiple noisy observations located within

389 the same grid and assimilation window is developed based on optimal estimation theory

390 (Miyazaki et al., 2012a). Previous studies have demonstrated the necessity of data-

391 thinning and dealiasing errors (Feng et al., 2020b; Zhang et al., 2009a). The super-

392 observation y_{new}, super-observation error r_{new} and corresponding simulation $x_{new,i}$

393 of the ith sample are calculated as follows:

$$1 \Big/ r_{new}^2 = \sum_{j=1}^m 1 \Big/ r_j^2 \tag{13}$$

$$y_{new} = \sum_{j=1}^m w_j\, y_j \Big/ \sum_{j=1}^m w_j \tag{14}$$

$$x_{new,i} = \sum_{j=1}^m w_j\, x_{ij} \Big/ \sum_{j=1}^m w_j \tag{15}$$

397 where j is the identifier of m observations within a super-observation grid; r_j is the

398 observational error of actual jth observation y_j ; x_{ij} represents a simulated

399 concentration using the ith prior emission sample corresponding to the jth observation;

400 and $w_j = 1 \Big/ r_j^2$ is the weighting factor. The super-observation error decreases as the

401 number of observations used within a super-observation increases. This method has

402 been used in our previous inversions using surface-based (Feng et al., 2020b) and

403   satellite-based (Jiang et al., 2021) observations.

404   In this study, the DA window was set to 1 day because the model needs a longer time

405   to integrate emission information into the concentration ensembles (Ma et al., 2019).

406   Due to the "super-observation" approach, only one assimilation is needed in one

407   assimilation window. In addition, due to the complexity of hourly emissions, it is very

408   difficult to simulate hourly concentrations that can match the observations well.

409   Although a longer DA window could allow more observations to constrain the emission

410   change of one grid, the spurious correlation signals of EnKF would attenuate

411   observation information with time (Bruhwiler et al., 2005; Jiang et al., 2021). Kang et

412   al. (2012) conducted OSSEs and demonstrated that due to the errors of transport and

413   increase the spurious correlation, a longer DA window (e.g., 3 weeks) would cause the

414   analysis system to blur out the essential emission information far away from the

415   observation. Therefore, daily mean simulations and observations are used in the EnSRF

416   algorithm, and daily emissions are optimized in this system.

417   EnKF is subject to spurious correlations due to the limited number of ensembles when

418   it is applied in high-dimensional atmospheric models, which can cause rank

419   deficiencies in the estimated background error covariance and filter divergence, and

420   further degrade analyses and forecasts (Wang et al., 2020). Covariance localization is

421   performed to reduce spurious correlations caused by the finite ensemble size

422   (Houtekamer and Mitchell, 2001). Covariance localization preserves the meaningful

423   impact of observations on state variables within a certain distance (cutoff radius) but

424   limits the detrimental impact of observations on remote state variables. The localization

425   function of Gaspari and Cohn function (Gaspari and Cohn, 1999) is used in this system,

426   which is a piecewise continuous fifth-order polynomial approximation of a normal

427   distribution. The optimal localization scale is related to the ensemble size, assimilation

428   window, dynamic system, and lifetime of a chemical species in the atmosphere. CO,

429   SO_2 and $PM_{2.5}$ are rather stable in atmosphere, with a lifetime more than 1 day.

430   According to the averaged wind speed (3.3 m/s, Table 4) and the length of DA window,

431   their localization scales are set to 300 km. In addition, NO_2 is rather reactive, with a

432 lifetime of approximately 10 hours in winter (de Foy et al., 2015), and PMC, which is

433 mainly from local sources, its residence time in the atmosphere is also short due to the

434 rapid deposition rate (Clements et al., 2014; Clements et al., 2016; Hinds, 1982). Their

435 localization scales are set to 150 km and 250 km, respectively.

436 **2.2 Prior emissions and uncertainties**

437 The anthropogenic emissions over China were taken from the 2016 Multi-resolution

438 Emission Inventory for China (MEIC 2016) (Zheng et al., 2018), while those over the

439 other regions of East Asia were obtained from the mosaic Asian anthropogenic emission

440 inventory (MIX) (Li et al., 2017). The spatial resolutions of both the MEIC and MIX

441 inventories are $0.25° \times 0.25°$, and they are both downscaled to match the model grid

442 spacing of 36 km. The spatial distributions of the CO, SO_2, NO_x, $PPM_{2.5}$ and PMC

443 emissions are shown in Figure 12. The daily emission inventory, which was arithmetic

444 averaged from the combined monthly emission inventory, was directly used in the EI

445 subsystem and employed as the prior emission of the first DA window in the EI

446 subsystem (Figure 1). During the simulations, the daily emissions were further

447 converted to hourly emissions. For all the species emitted from area sources, we

448 converted them to hourly using a same diurnal profile (Figure S2), and for the point

449 source, we assumed that there was no diurnal change. MEIC 2012 was used as an

450 alternative a priori over China to investigate the impact of different prior emissions on

451 the optimized emissions. The Model of Emissions of Gases and Aerosols from Nature

452 (MEGAN) (Guenther et al., 2012) was used to calculate time-dependent biogenic

453 emissions. It was also driven by the WRF model in this study. Biomass burning

454 emissions were not included because they have little impact across China during the

455 study period (Zhang et al., 2020).

456 During the inversion cycles, the inverted emissions of different members converge

457 gradually, and the ensemble-estimated error covariance matrix is arithmetically likely

458 to be underestimated. To avoid this, considering the compensation of model errors and

459 comparable emission uncertainties from one day to the next, we impose the same

460 uncertainty on emissions at each DA window. As mentioned above, the optimized

461   emissions of the current DA window are transferred to the next DA window as prior

462   emissions. The technology-based emission inventory developed by Zhang et al. (2009b),

463   basically using the same method as MEIC, shows that the emissions of PMC and PPM$_{2.5}$

464   have the largest uncertainties, followed by CO, and finally SO$_2$ and NO$_x$. Therefore, the

465   uncertainties in this study are set to 40%, 40%, 30%, 25%, and 25%. However, previous

466   studies have shown that the inversely estimated CO and PMC emissions could exceed

467   100% higher than the bottom-up emissions (MEIC) in certain areas (Feng et al., 2020b;

468   Ma et al., 2019). According to the extent of underestimation, we set an uncertainty of

469   100% for both the CO and PMC emissions at the beginning of the three DA windows

470   to quickly converge the emissions. The mean emission analysis is generally minimally

471   sensitive to the uncertainty setting in our assimilation cycle method (Feng et al., 2020;

472   Gurney et al., 2004; Miyazaki et al., 2012a) because the inversion errors of the current

473   window could be transferred to the next window for further optimization (Sect. 4.3).

2.3 Observation data and errors

475   Hourly averaged surface CO, SO$_2$, NO$_2$, O$_3$, PM$_{2.5}$ and PM$_{10}$ observations from 1504

476   national control air quality stations were assimilated in this system, which were

477   obtained from the Ministry of Ecology and Environment of the People's Republic of

478   China (http://106.37.208.233:20035/, last access: 25 June 2020). These sites are

479   distributed over most of central and eastern China and become denser near metropolitan

480   areas (see Figure 2). Value-range and time-continuity checks were performed to ensure

481   data quality. Value-range checks were mainly performed to eliminate unrealistic or

482   unrepresentative observations. Only observations within the subjectively selected

483   threshold range were assimilated (Table 2). A time-continuity check was performed to

484   eliminate gross outliers and a sudden anomaly using a function of $max(|O(t) -$

485    $O(t \pm 1)|) \leq f(t)$, where $O(t)$ and $O(t \pm 1)$ represent observations at time t and

486    $t \pm 1$, respectively, and $f(t) = T_a + T_b \times O_t$. That means that both concentration

487   differences between time *t* and time *t+1* and *t-1* should be less than $f(t)$. T_b is fixed

488   to 0.15, and the section of T_a is given in Table 2, which is determined empirically

489   according to the time series change of concentration at each site. It should be noted that,

490 to avoid potential cross-correlations, we assimilated PM$_{2.5}$ and PMC. Additionally, in

491 the EI subsystem, the observations within each city were averaged to thin the data

492 density, reduce the error correlation and increase the spatial representation (Houtekamer

493 and Mitchell, 2001; Houtekamer and Zhang, 2016). Finally, 336 city sites are available

494 across the mainland of China, in which 311 cities' data were selected for assimilation

495 and the remaining 25 were selected for independent validation (Figure 2). In the IA

496 subsystem, due to the small horizontal correlation scale (Figure 3), to obtain more

497 extensive observation constraints, all site observations were assimilated to provide a

498 good IC for the next emission inversion.

499 The observation error covariance matrix (**R**) includes both measurement and

500 representation errors. The measurement error ε_0 is defined as follow:

$$\varepsilon_0 = ermax + ermin \times \Pi_0 \tag{16}$$

502 where $ermax$ is a base error, and Π_0 denotes the observed concentration. These

503 parameters for different species are listed in Table 2, which are determined according

504 to Chen et al. (2019), Feng et al., (2018) and Jiang et al. (2013b).

505 The representative error depends on the model resolution and the characteristics of the

506 observation locations, which were calculated using the equations of Elbern et al. (2007)

507 defined as follows:

$$\varepsilon_r = \gamma \varepsilon_0 \sqrt{\Delta l / L} \tag{17}$$

509 where γ is a tunable parameter (here, γ=0.5), Δl is the grid spacing (36 km), and L

510 indicates the radius (here, 3 km for simplification) of influence area of an observation.

511 The total observation error (r) is defined as follows:

$$r = \sqrt{\varepsilon_0{}^2 + \varepsilon_r{}^2} \tag{18}$$

513

514

 Table 2. Parameters of quality control and measurement error

Parameter	CO mg m^{-3}	SO$_2$ μg m^{-3}	NO$_2$ μg m^{-3}	O$_3$ μg m^{-3}	PM$_{2.5}$ μg m^{-3}	PMC μg m^{-3}
value-range	0.1-12	1-800	1-250	1-250	1-800	1-900
time-continuity (T_a)	2.5	160	70	80	180	180
ermax	0.05	1	1	1	1.5	1.5
ermin	0.5%	0.5%	0.5%	0.5%	0.75%	0.75%

516

3 Experimental design

RAPAS was conducted according to the procedure and settings described in Sect. 2. December is one of the months with most severe air pollution, while July is one of the least polluted months in China. Therefore, this study mainly tested the performance of the RAPAS system in these two months. For December, the IA subsystem was run from 26 to 31 November 2016 with a 6-hour interval cycling assimilation to optimize ICs (ICDA). A better IC at 0000 UTC on December 1 can be obtained by 5-day high-frequency cycling assimilation and atmospheric mixing. Then the EI subsystem was run for December 2016 with a 1-day assimilation window to optimize emissions (EMDA). For July, the system also operated in the same way as for December. It needs to be noted that due to the stronger atmospheric oxidation, the lifetime of NO2 in July is significantly shorter than that in December, thus we adopted a smaller localization scale for NO2 (80 km). Both assimilation experiments use the combined prior emission inventories of 2016 as described in Sect. 2.2, and the emission base year coincides with the research stage. An Observing Systems Simulation Experiment (OSEE) was conducted to evaluate the performance of the RAPAS system, which has been widely used in previous assimilation systems development (Daley, 1997). In the OSSE experiment, we used the MEIC 2016 inventory as a "true" emission, and reduced the "true" emission by 30% over the mainland of China as a prior emission. The simulations simulated using the "true" emission and sampled according to the locations and times

of the real observations were used as artificial observations. The observation errors are the same as those in EMDA. To evaluate the IC improvements from the IA subsystem, an experiment without 3DVAR (NODA) is conducted with the same meteorological fields and physical and chemistry parameterization settings as those of the ICDA. To evaluate the posterior emissions of the EI subsystem, two parallel forward modeling experiments are performed for December 2016, namely, a control experiment (CEP) with prior (MEIC 2016) emissions and a validation experiment (VEP) with posterior emissions. Both experiments use the same initial field at 0000 UTC on December 01 generated through the IA subsystem. Similar to the above, the only differences between CEP and VEP are emissions. Table 3 gives a summary of different emission inversion experiments conducted in this study.

To investigate the robustness of our system, 8 sensitivity tests (from EMS1 to EMS8, see Table 3) are performed. These experiments are all based on EMDA. In EMS1, rather than forward simulated using the optimized emissions of the previous DA window in EMDA, the initial fields of each DA window were first taken from forward simulation with the prior emissions of the previous DA window, and then optimized using the 3DVAR algorithm and the observations at the corresponding moment as mentioned in Sect. 2.3. The objective of this experiment is to investigate the advantages of the "two-step" calculation scheme in the EI subsystem as introduced in Sect. 2.1. EMS2 uses MEIC 2012 as the original prior emission in China, aiming to investigate the impact of different prior inventories on the estimates of emissions. Four other experiments, namely EMS3-6, aim to test the impact of different prior uncertainty settings, in which, the prior uncertainties are reduced by -50% and -25%, and increased by 25% and 50%, respectively. EMS7 aims to evaluate the impact of observation errors on emission estimates, in which all the observation errors are magnified twice. The last EMS8 experiment aims to evaluate the impact of IC optimization of the first window on emission estimates, in which the ICs were taken from a 5-day spin-up simulation. Eight forward modeling experiments (VEP1, VEP2, …, VEP8) were also performed with posterior emissions of EMS1 to EMS8 to evaluate their performances, respectively.

566 **Table 3**. Emission inversion and sensitivity experiments conducted in this study

Exp. Type	Exp. Name	Period	IC of the first DA Window	ICs of the subsequent DA window	Emission
Assimilation	EMDA	1-31 December	0000 UTC on December 1, taken from ICDA	Forecast with posterior emissions in the previous window	MEIC 2016 for December (the first DA window), optimized emissions of the previous window (other DA windows)
	OSSE	1-31 December	The same as EMDA	The same as EMDA	The same as EMDA, but with a decrease of 30% for CO, SO_2, NO_x, $PPM_{2.5}$, and PMC
Sensitivity	EMS1	1-31 December	The same as EMDA	Forecast with prior emissions in the previous window and 3DVAR assimilation	The same as EMDA
	EMS2	1-31 December	The same as EMDA	The same as EMDA	The same as EMDA, but for EMIC 2012
	EMS3-6	1-31 December	The same as EMDA	The same as EMDA	The same as EMDA, but with a $\pm$ 25% or $\pm$ 50% of default uncertainty
	EMS7	1-31 December	The same as EMDA	The same as EMDA	The same as EMDA, but with a +100% of default observation errors
	EMS8	1-31 December	0000 UTC on December 1, taken from ICNO	The same as EMDA	The same as EMDA

567

568

569

4 Results

4.1 Evaluations

4.1.1 Simulated meteorological fields

In the RAPAS system, the inversion approach attributes all the biases between the simulated and observed concentrations to the emissions. The meteorological fields dominate the physical and chemical processes of the air pollutants in the atmosphere, and thus their simulation accuracy would significantly affect the estimates of emissions in this study. To quantitatively evaluate the performance of the WRF simulations, the mean bias (BIAS), root mean square error (RMSE), and correlation coefficient (CORR) were calculated against the surface meteorological observations measured at 400 stations and the planetary boundary layer height (PBLH) calculated using the sounding data at 92 sites. The surface observations were obtained from the National Climate Data Center (NCDC) integrated surface database (http://www.ncdc.noaa.gov/oa/ncdc.html, last access: 25 October 2021), and the sounding data were obtained from the website of the University of Wyoming (http://weather.uwyo.edu/upperair/sounding.html, last access: 10 March 2022). The sounding data are in 12 hours interval. The observed PBLH were calculated using the sound data through the bulk Richardson number method (Richardson et al., 2013). The spatial distribution of the meteorological stations is shown in Figure 2. The simulated temperature at 2 m (T2), relative humidity at 2 m (RH2), wind speed at 10 m (WS10), and PBLH from 26 November to 31 December 2016 are evaluated against the observations. Table 4 summarizes the statistical results of the evaluations of the simulated meteorological parameters. Overall, the T2, RH2 and PBLH are slightly underestimated, with biases of -0.1 °C, -3.8% and -41.1 m, respectively. The CORRs are approximately 0.98 for T2, 0.94 for RH2 and 0.90 for PBLH, showing good consistency between the observations and simulations. The WS10 is overestimated, with a bias of 0.7 m/s and an RMSE of 0.8 m/s, but is better than many other studies (Chen et al., 2016; Jiang et al., 2012a; Jiang et al., 2012b). Therefore, WRF can generally reproduce the meteorological conditions sufficiently in

598   terms of their temporal variation and magnitude over China, which is adequate for our

599   inversion estimation.

600   **Table 4**. Statistics comparing the simulated and observed 10-m wind speed (WS10), 2-

601   m temperature (T2), and 2-m relative humidity (RH2), and planetary boundary layer

602   height (PBLH).

Variable Met.	No. of sites	Mean Obs.	Mean Sim.	BIAS	RMSE	CORR
WS10 (m/s)	400	2.6	3.3	0.7	0.8	0.72
T2 (°C)	400	2.9	2.8	-0.1	0.7	0.98
RH2 (%)	400	66.3	62.6	-3.8	5.2	0.94
PBLH (m)	92	267.5	226.4	-41.1	50.4	0.90

603   * BIAS, mean bias; RMSE, root mean square error; CORR, correlation coefficient

604   **4.1.2 Initial fields**

605   Figure 4 shows the evaluations of the analyzed concentrations of the 6 species against

606   surface observations. For comparison, the evaluations of the simulations without

607   3DVAR (NODA) are also shown in Figure 4. The simulations of the NODA experiment

608   (red dots) are scattered on both sides of a central line, as large systematic biases remain

609   across many measurement sites. Conversely, the ICDA experiment (blue dots) shows

610   much better agreement with observations than those from NODA. The statistics show

611   that there are large systematic biases in the NODA simulations, with large RMSEs and

612   small CORRs for all species, especially for CO and PMC. After the assimilation of

613   surface observations, the RMSE of CO decreases to 0.7 mg m^{-3}, and those of SO_2, NO_2,

614   O_3, $PM_{2.5}$ and PMC decrease to 22.0, 12.0, 9.6, 20.5 and 19.6 μg m^{-3}, respectively, with

615   respective reduction rates of 50.0%, 73.1%, 61.0%, 64.7%, 69.5%, and 60.8%

616   compared to the ones of the NODA (Table 5). The CORRs of ICDA increase by 290.0%,

617   291.3%, 55.4%, 87.2%, 130.0% and 214.8% to 0.78, 0.90, 0.87, 0.88, 0.92 and 0.85,

618   respectively. These statistics indicate the initial fields of the ground level have been

619   significantly improved. However, due to the lack of observations, we still do not know

the simulation bias in the upper-middle boundary layer. Although concentrations at high

altitudes can be constrained by ground-based observations through vertical correlations,

the effect is limited, so the bias is still non-negligible.
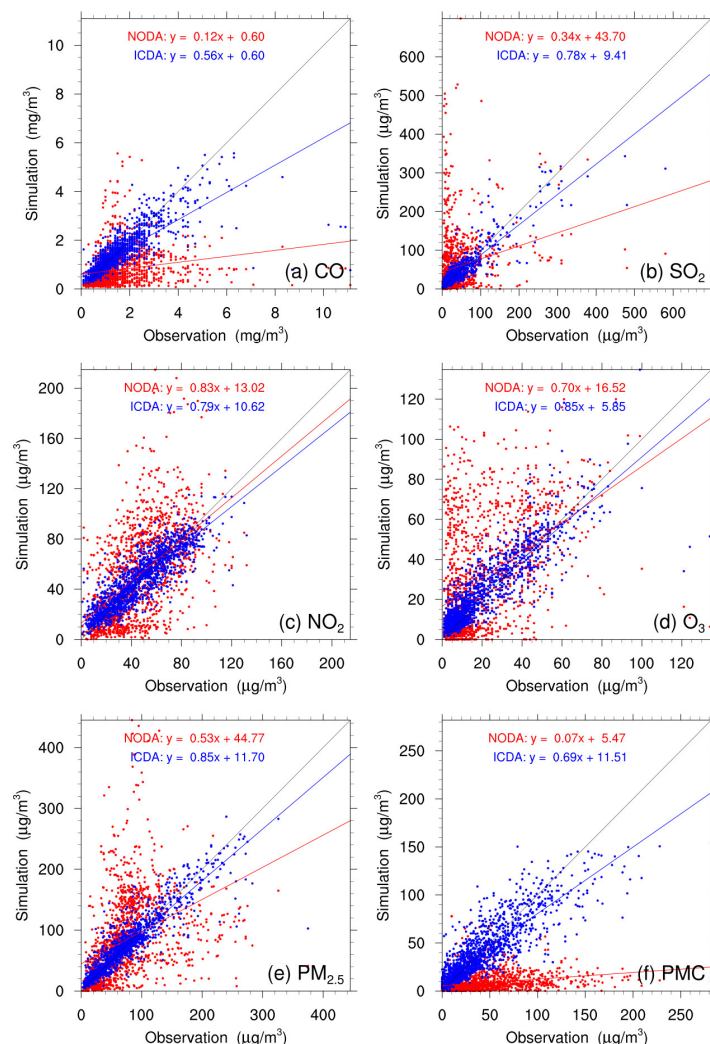
Figure 4. Scatter plots of simulated versus observed (a) CO, (b) SO₂, (C) NO₂, (d) O₃,

(e) PM$_{2.5}$ and (f) PMC mass concentrations at 0000 UTC on December 1 initializations

from the background (red) and analysis (blue) fields.

Table 5. Comparisons of the surface CO, SO$_2$, NO$_2$, O$_3$, PM$_{2.5}$ and PMC mass concentrations from the control and assimilation experiment against observations aggregated over all analysis times. CO unit: mg m^{-3}; others units: μg m^{-3}.

Species	Exp. Name	Mean Obs.	Mean Sim.	BIAS	RMSE	CORR
CO	NODA	1.5	0.8	-0.7	1.4	0.20
	ICDA		1.5	-0.1	0.7	0.78
SO$_2$	NODA	36.3	56.0	19.7	81.7	0.23
	ICDA		37.8	1.5	22.0	0.90
NO$_2$	NODA	45.8	51.1	5.3	30.8	0.56
	ICDA		47.0	1.1	12.0	0.87
O$_3$	NODA	20.5	30.8	10.4	27.2	0.47
	ICDA		23.3	2.8	9.6	0.88
PM$_{2.5}$	NODA	70.9	82.2	11.3	67.3	0.40
	ICDA		71.8	0.9	20.5	0.92
PMC	NODA	43.5	8.5	-35.0	50.0	0.27
	ICDA		41.6	-1.9	19.6	0.85

* BIAS, mean bias; RMSE, root mean square error; CORR, correlation coefficient

4.1.3 Posterior emissions

Due to mismatched spatial scales, it is difficult to directly evaluate the optimized emissions against observations. Generally, we indirectly validate them by comparing the forward simulated concentrations using the posterior emissions against atmospheric measurements (e.g., Jiang et al. (2014), Jin et al. (2018), and Peters et al. (2007)). Figure 5 shows the spatial distributions of the mean biases between the simulated gaseous pollutants using prior and posterior emissions and assimilated observations. In the CEPs, for each species, the distribution of biases is similar to the increments in background fields constrained through 3DVAR as shown in Figure S3. For example, almost all sites have large negative biases for CO, while for SO$_2$ and NO$_2$, positive biases are mainly distributed over the North China Plain (NCP), Yangtze River Delta (YRD), Sichuan Basin (SCB) and Central China, and negative biases are over the rest of the areas. After constraining with observations, the biases of all the 3 gaseous air pollutants are

648 significantly reduced in most sites. For CO, the biases at 62% of the sites decreased to
649 absolute values less than 0.2 mg m^{-3}, and for SO_2 and NO_2, the biases at 52% and 47%
650 of the sites were within ±4 μg m^{-3}. However, large negative biases are still observed in
651 part of western Chinas, indicating that the uncertainties of the posterior emissions are
652 still large in western China, which may be attributed to the large biases in prior
653 emissions and to the relatively limited observation. Overall, the statistics show that
654 there are different levels of improvements at 92%, 85% and 85% of the total 311
655 assimilation sites for CO, SO_2 and NO_2, respectively. The small amount of sites with
656 worse performance may be related to the overadjusted emissions by EI or contradictory
657 adjustments caused by opposite biases in adjacent areas.

658 Table 6 lists the statistical results of the evaluations averaged over the whole mainland
659 of China. For CO, the mean bias is -0.8 mg m^{-3} with the prior emissions, while it
660 substantially reduces to -0.1 mg m^{-3} with a reduction rate of 89.6% when simulating
661 with the posterior emissions. Additionally, the RMSE decreases by 48.1% from 1.08 to
662 0.56 mg m^{-3}, and the CORR increases by 76.1% from 0.46 to 0.81. For SO_2 and NO_2,
663 the regional mean biases slightly increase as the positive/negative biases among
664 different sites might be offset. However, the RMSEs decrease to 17.7 and 12.3 μg m^{-3},
665 respectively, which are 58.3% and 50.8% lower than those of CEPs, and the CORRs
666 increase by 125.6% and 35.4%, both reaching up to 0.88, indicating that EI has
667 significantly improved the NO_x and SO_2 emission estimates.

668
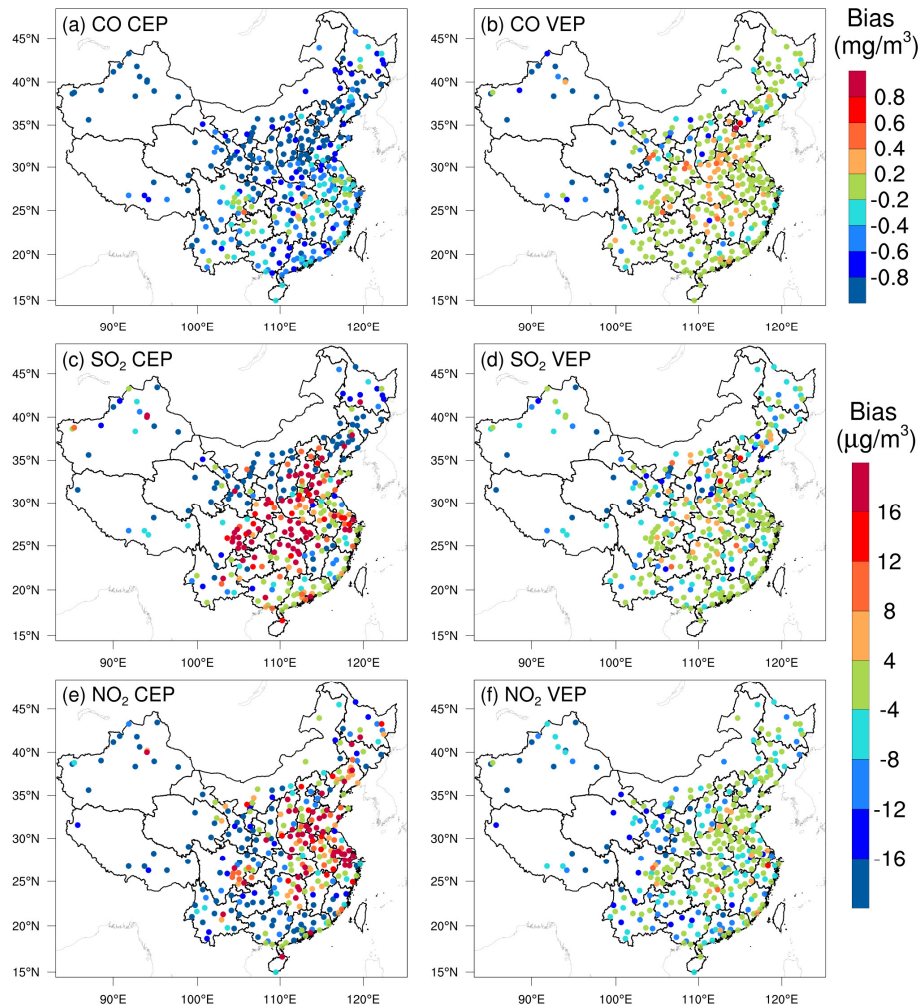
Figure 5. Spatial distribution of the BIAS of the simulated (a, b) CO, (c, d) SO_2 and (e, f) NO_2 with prior (left, CEP) and posterior (right, VEP) emissions. CO unit: mg m^{-3}; SO_2 and NO_2 units: μg m^{-3}.

Figure 6 shows the spatial distributions of the mean biases of simulated $PM_{2.5}$ and PMC evaluated against the assimilated observations. Similarly, the CEP simulations do not perform well. There are widespread underestimations across the country, with mean biases of -24.0 and -32.4 μg m^{-3}. After data assimilation, the performance of VEP simulations is significantly improved. The biases decrease by 72.1% and 90.4% to -6.7 and -3.1 μg m^{-3}, the RMSEs decrease by 41.2% and 40.7% to 29.6 and 24.6 μg m^{-3}, and the CORRs increase by 35.9% and 176.0% to 0.87 and 0.69 for $PM_{2.5}$ and PMC, respectively. Overall, 89.6% and 97.2% of the assimilation sites are improved for $PM_{2.5}$

680 and PMC, respectively. However, compared with the results of the 3 gaseous pollutants,

681 there are sites with large biases scattered throughout the whole domain. Besides the

682 potential overadjusted or contradictory adjustments of emissions as in the 3 gas species,

683 It may also be related to the complex precursors and complex homogeneous and

684 heterogeneous chemical reactions and transformation processes of secondary PM$_{2.5}$,

685 and the fact that we do not simulate the time variation of dust blowing caused by wind

686 speed for PMC due to the lack of land cover data that is compatible with the CMAQ

687 dust module and agricultural activities data to identify dust source regions.
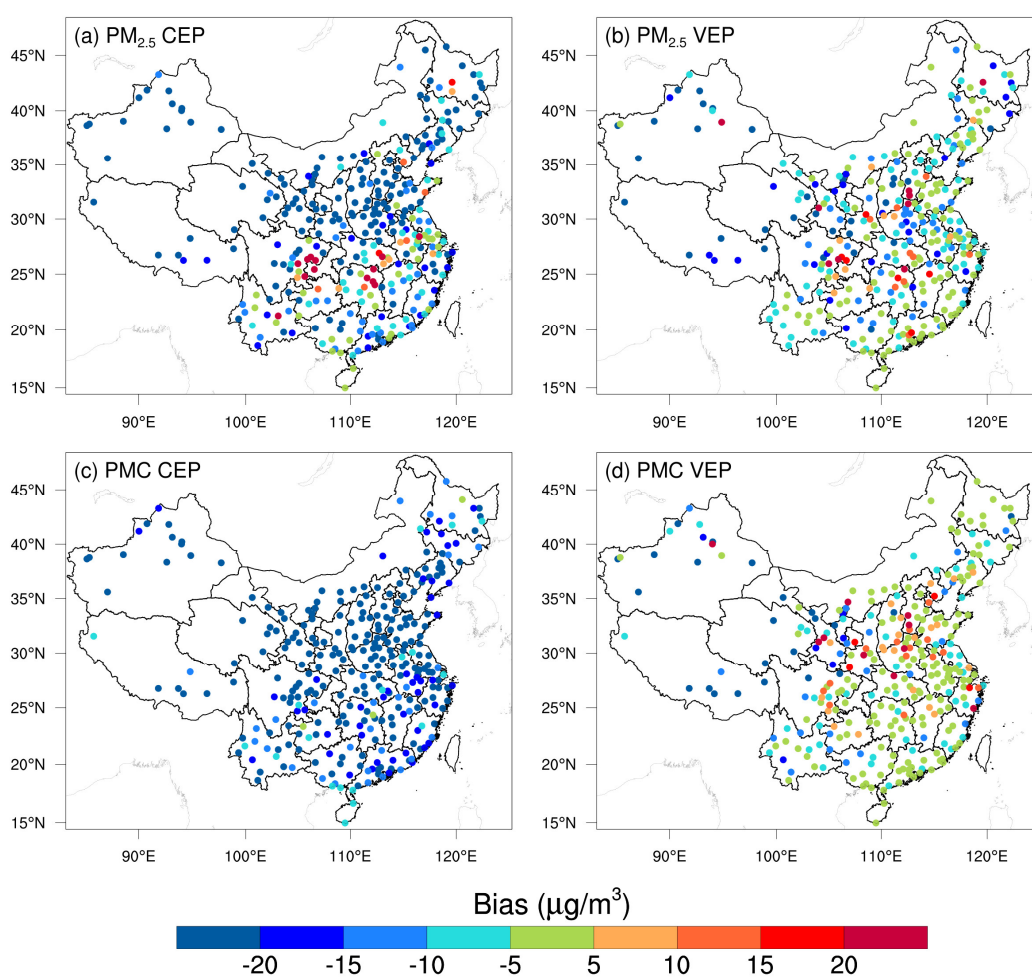
688

689 **Figure 6**. Same as in Figure 5 but for PM$_{2.5}$ and PMC.

690 Figure 7 and Figure 8 show the spatial distributions of the biases calculated against the

691 independent observations for the 5 species. With posterior emissions, the decreasing

692   ratios of RMSEs range from 26.7% to 42.0%, and the CORRs increase by 13.7-59.0%

693   to 0.62-0.87. Overall, the biases at the independent sites are similar or slightly worse

694   than those at the assimilated sites, which is reasonable since the closer to the assimilated

695   site the independent sites are, the more constraints of observation information can be

696   obtained, and the improvements in optimized state variables of the model are more

697   significant. For example, generally, the transmission distance of NO_2 is relatively short,

698   and remote cities with small emission correlations to the cities with assimilated

699   observations are relatively less constrained, resulting in only a 26.7% decrease in the

700   RMSE.
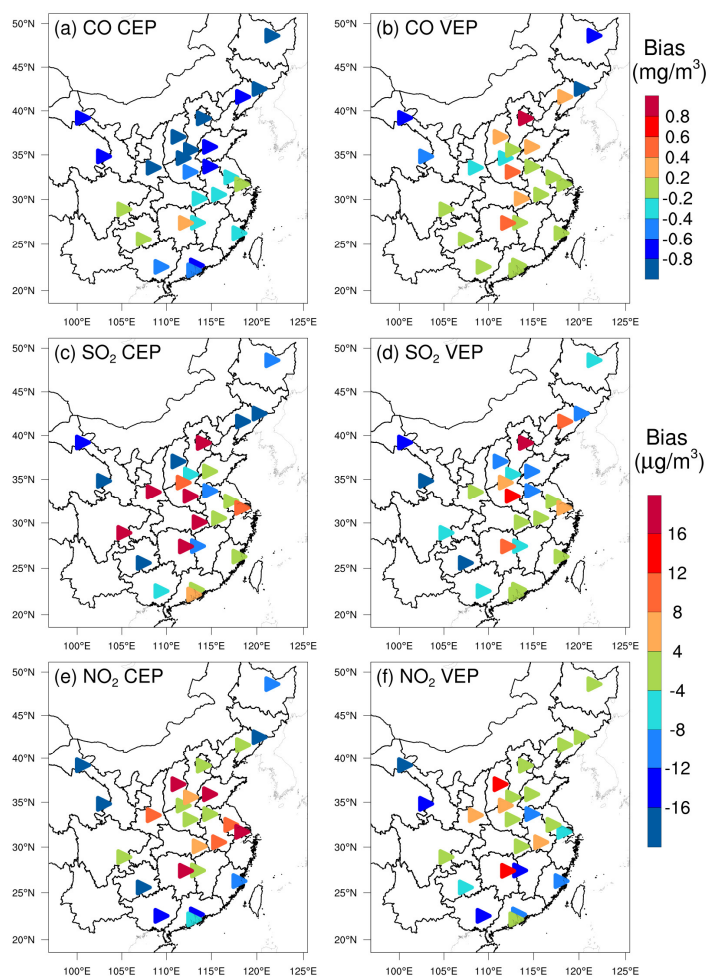
701

702   **Figure 7**. As in Figure 5 but for the independent validation.

703
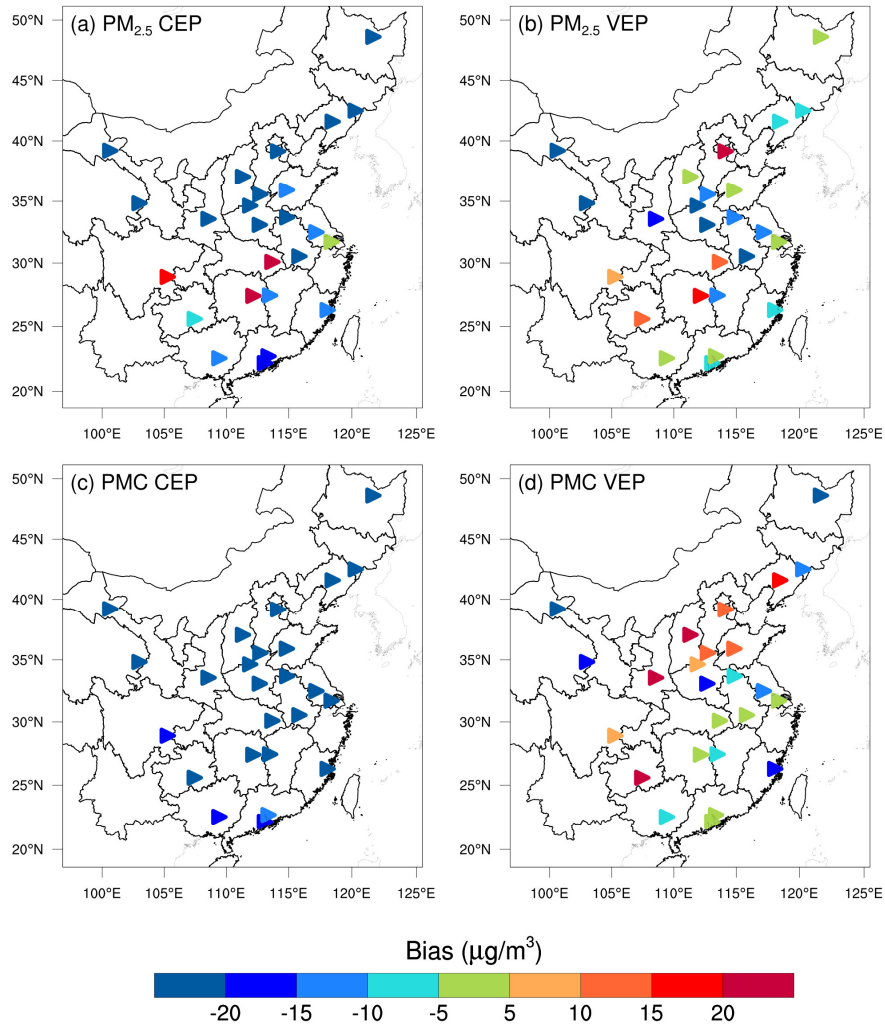
Figure 8. As in Figure 6 but for the independent validation.

Compared with the previous studies, Tang et al. (2013) conducted inversion of CO
emissions over Beijing and the surrounding areas, the improvements (Table 6) in the
RMSE (37-48% vs. 30-51%) and the CORR (both studies ~ 0.81) are comparable, but
the biases here could decrease by 90-97%, which is much greater than their 48-64%
reductions. Additionally, Chen et al. (2019) showed that the RMSE of simulated SO_2
with updated SO_2 emissions decreased by 4.2-52.2% for different regions, and the
CORR only increased to 0.69 at most. The improvement is relatively smaller than our
results, which may be due to the insufficient adjustment of emissions caused by the
underestimated ensemble spread through the inflation method. The better performance
in this study may be related to our inversion process that makes the optimized emissions

715 of the current DA window propagate to the next DA window for further correction.

716 **Table 6**. Statistics comparing the pollution concentrations from the simulations with
717 prior (CEP) and posterior (VEP) emissions against assimilated and independent
718 observations, respectively. CO unit: mg m^{-3}; others units: μg m^{-3}.

Species	Mean Obs.	Mean Sim.		BIAS		RMSE		CORR	
		CEP	VEP	CEP	VEP	CEP	VEP	CEP	VEP
Against assimilated observations									
CO	1.43	0.66	1.36	-0.77	-0.08	1.08	0.56	0.46	0.81
SO$_2$	32.5	34.4	28.4	1.9	-4.1	42.4	17.7	0.39	0.88
NO$_2$	43.8	40.8	39.0	-2.9	-4.8	25.0	12.3	0.65	0.88
PM$_{2.5}$	77.0	53.1	70.3	-24.0	-6.7	50.3	29.6	0.64	0.87
PMC	40.5	8.1	37.5	-32.4	-3.1	41.5	24.6	0.25	0.69
Against independent observations									
CO	1.54	0.79	1.52	-0.75	-0.02	1.15	0.72	0.59	0.82
SO$_2$	40.6	39.2	37.3	-1.3	-3.2	44.3	27.2	0.57	0.87
NO$_2$	50.2	50.0	47.5	-0.3	-2.7	21.7	15.9	0.73	0.83
PM$_{2.5}$	91.5	64.6	84.1	-26.9	-7.4	64.1	37.2	0.62	0.87
PMC	42.0	9.2	40.4	-32.8	-1.6	39.3	26.6	0.39	0.62

719 * BIAS, mean bias; RMSE, root mean square error; CORR, correlation coefficient

4.1.4 Uncertainty reduction

721 The uncertainty reduction rate (UR) is another important quantity to evaluate the
722 performance of RAPAS and the effectiveness of in-situ observations in this system
723 (Chevallier et al., 2007; Jiang et al., 2021; Takagi et al., 2011). Following Jiang et al.
724 (2021), the UR is calculated as

$$UR = (1 - \frac{\sigma_{posterior}}{\sigma_{prior}}) \times 100 \qquad (19)$$

726 where $\sigma_{posterior}$ and σ_{prior} are the posterior and prior uncertainties, respectively,
727 which were calculated using the standard deviations of the prior and posterior
728 perturbations (Text S3). Figure 9 shows the URs averaged in each province and the
729 whole mainland China. The URs vary with species, and among the 5 species of
730 emissions, the uncertainties of the PPM$_{2.5}$ and PMC are greatly reduced, while the UR
731 of NO$_x$ emission is lowest, that is because the URs are closely related to the magnitude

settings of prior uncertainties (Jiang et al., 2021). For the whole mainland China, the uncertainties are reduced by 44.4%, 45.0%, 34.3%, 51.8% and 56.1% for CO, SO_2, NO_x, $PPM_{2.5}$ and PMC, respectively. For one species, it also varies across provinces. The URs are usually related to observation coverage, which means that the more observation constraints there are, the more the URs decrease. Additionally, the URs may also relate to emission distributions. Generally, the URs are more significant in the provinces where the observations and emissions are both relatively concentrated (e.g., Tibet), while they are much lower in where the emissions are scattered or relatively uniform, but the observations are only in large cities, even though there are many more observations than other provinces.
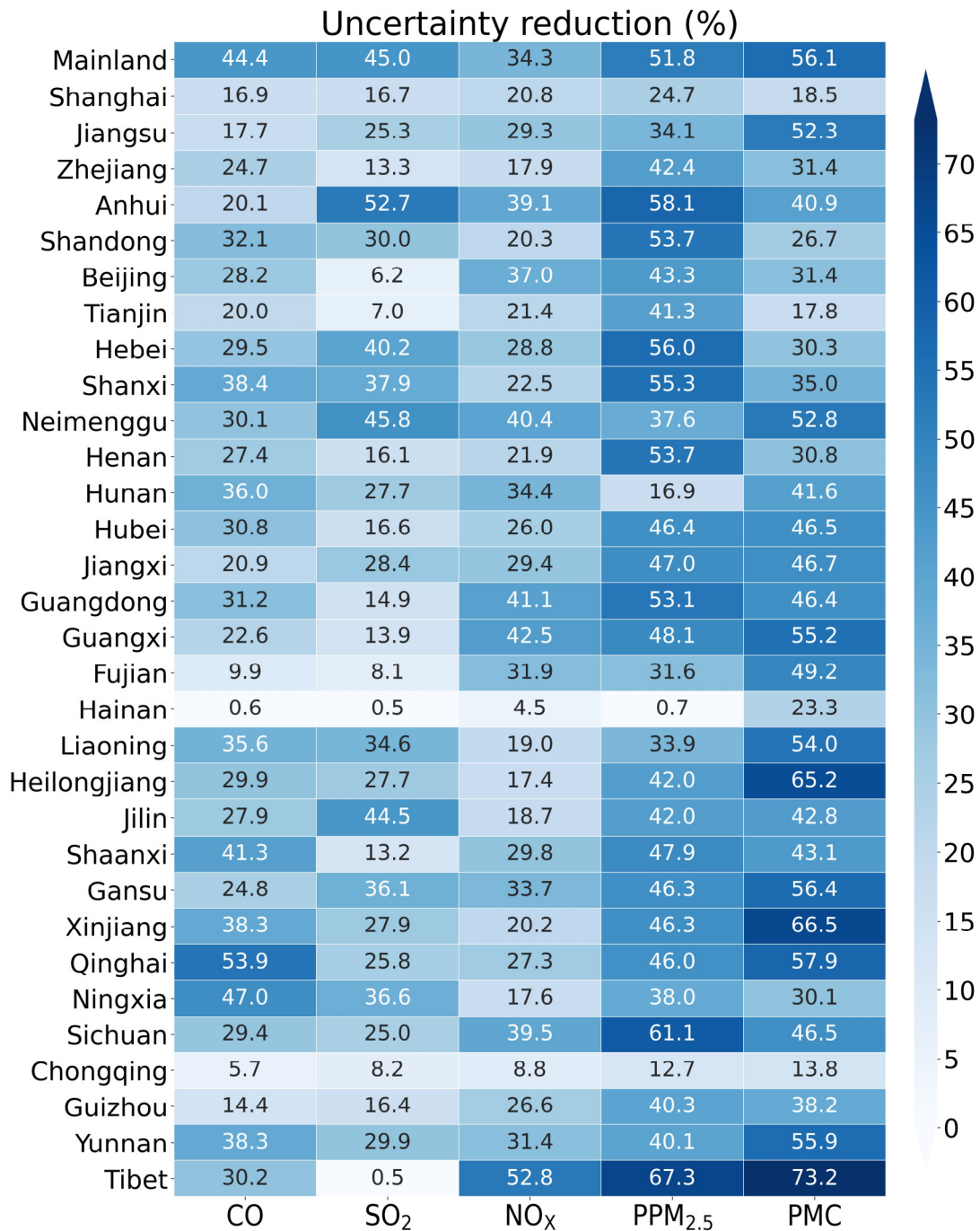
Figure 9. Time-averaged posterior emission uncertainty reduction (%) indicated by the standard deviation reduction of total emissions per province calculated by prior and posterior ensembles.

4.1.5 Evaluation using chi-squared statistics

To diagnose the performance of the EnKF analysis, the chi-squared (χ^2) statistics was calculated, which is generally used to test whether the prior ensemble mean RMSE with

749 respect to the observations is consistent with the prior "total spread" (square root of the

750 sum of ensemble variance and observation error variance). Following Zhang et al.

751 (2015), for the tth window, χ^2 is defined as

$$\chi_t^2 = (\boldsymbol{y} - \boldsymbol{H}\overline{\boldsymbol{X^b}})^T (\boldsymbol{H}\boldsymbol{P^b}\boldsymbol{H}^T + \boldsymbol{R})^{-1} (\boldsymbol{y} - \boldsymbol{H}\overline{\boldsymbol{X^b}}) \qquad (20)$$

753 Figure 10 shows the time series of the relative changes between the prior and posterior

754 emissions and the χ^2 statistics. There are relatively large adjustments of emissions in

755 the first three windows, especially for PMC. After that, the optimality of the five species

756 reaches a more optimal state with successive emission inversion cycle. The χ^2 statistics

757 shows a similar variation characteristics with the daily changes in the emissions. The

758 χ^2 value is slightly greater than 1, indicating that the uncertainties from error covariance

759 statistics do not fully account for the error in the ensemble simulations. A similar

760 situation also appeared in Chen et al. (2019). Further investigations should be

761 conducted to generate larger spreads by accounting for the influence of model errors.

762 Since we imposed a same uncertainty of prior emission at each DA window to partially

763 compensate for the influence of model errors, χ^2 statistics showed small fluctuations,

764 indicating that the system updates emissions consistently and stably.

765

766
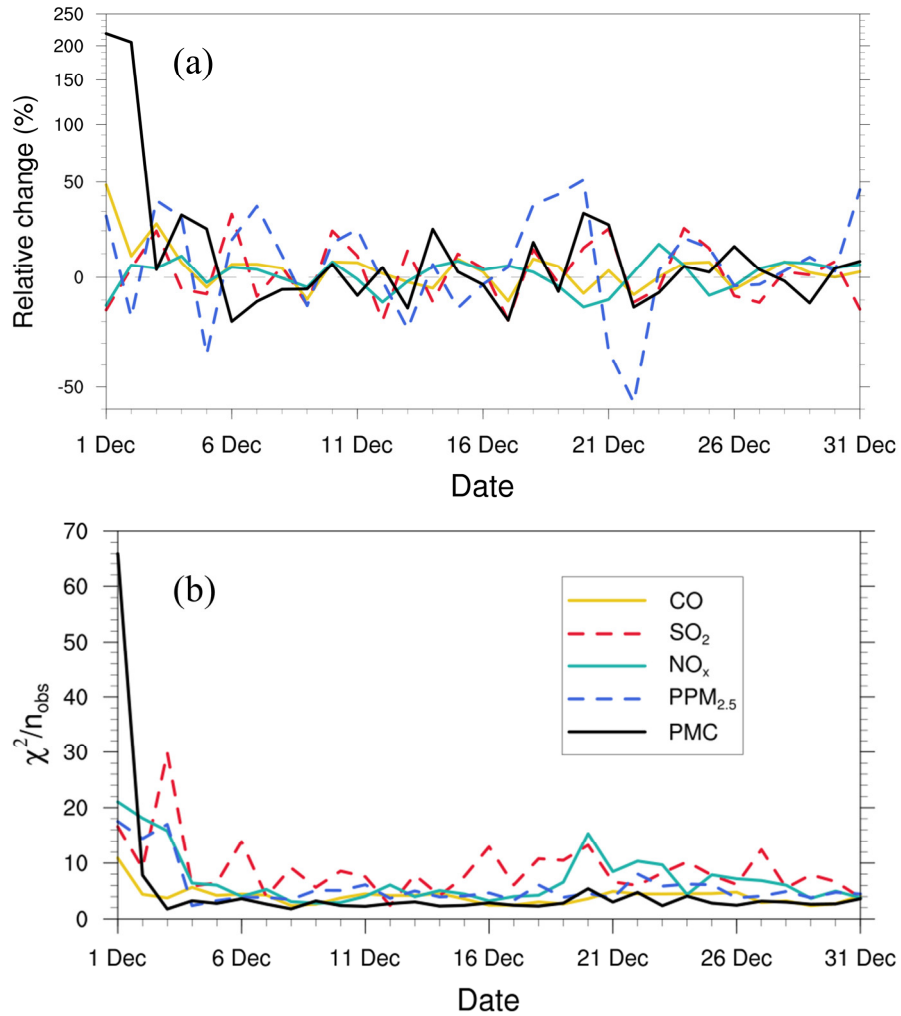
Figure 10. Relative changes (a) in a posteriori emission estimates of CO, SO$_2$, NO$_x$, PPM$_{2.5}$ and PMC, and χ^2 statistics (b) of these state vectors in each window.

4.1.6 Evaluation using OSSE

Figure 11 shows the spatial distribution of the error reduction in the posterior emissions of the five species. It can be found that after inversion, in most areas, the emission errors can be reduced by more than 80%, especially in the central and eastern regions with dense observation sites, while in remote areas far away from cities, due to the sparse observation sites, the emission errors are still not well adjusted. Overall, the error reduction rates of CO, SO$_2$, NO$_x$, PPM2.5, and PMC are 78.4%, 86.1%, 78.8%, 77.6%, and 72.0%, respectively, indicating that with the ground in-situ observations in China, RAPAS can significantly reduce emission errors, thus has good performance in

778 emission estimates.

779
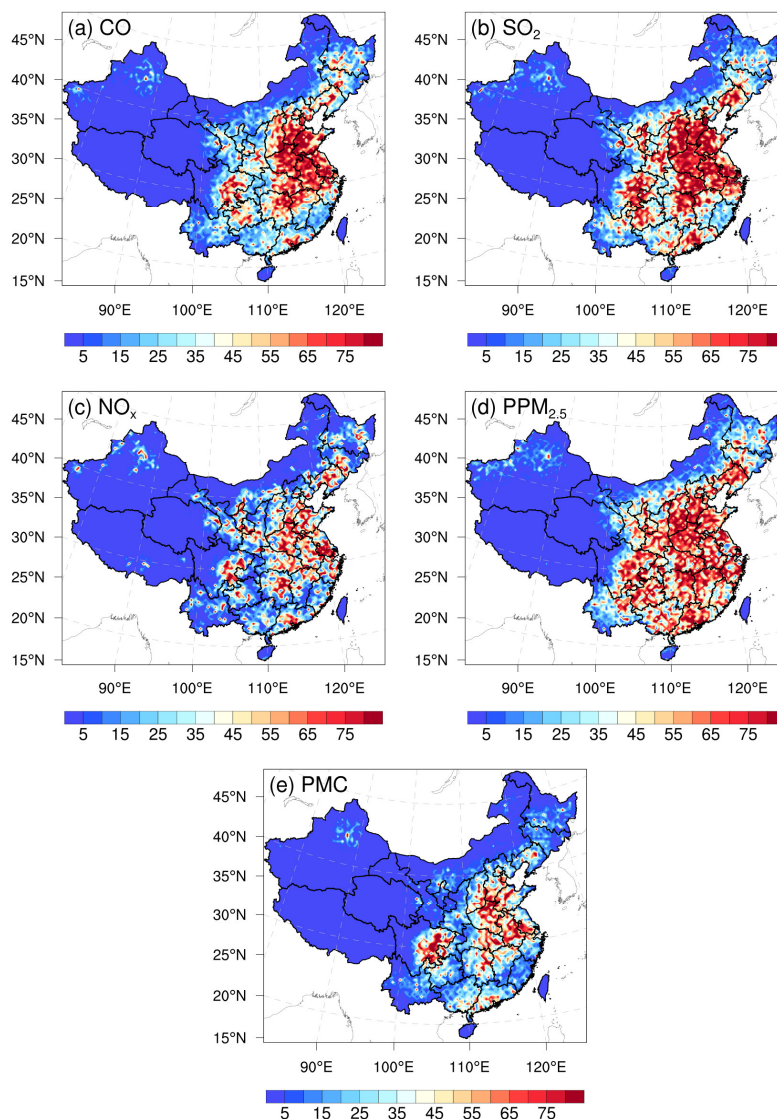
Figure 11 Spatial distribution of the error reduction (%) of posterior emissions in the OSSE.

4.2 Inverted emissions

Figure 12 shows the spatial distribution of the temporal averaged prior and posterior emissions and their differences of the emissions in December 2016. It should be noted that the emissions outside China were masked, since the observation sites are all within China in this study, there is little change in the emissions outside China. Higher emissions are mainly concentrated in central and eastern China, especially in the NCP, YRD, and PRD, and lower emissions occur across Northwest and Southern China.

Compared with the prior emissions, posterior CO emissions are considerably increased across most areas of mainland China, especially in northern China, with an overall increase of 129%. Notable underestimation of the prior emissions is also confirmed by previous inversion estimations (Feng et al., 2020b; Tang et al., 2013; Wu et al., 2020) and model evaluations (Kong et al., 2019b). For SO_2, the emission increases mainly occur in Northeast China, Shanxi, Ningxia, Gansu, Fujian, Jiangxi and Yunnan provinces. In SCB, Central China, YRD, and part of NCP, the emissions are significantly reduced. For national total, the SO_2 emission is increased by 20%. For NO_x, although the increment of national total emissions is small, only about 5%, large deviations still exist on regional scale. Obviously, the emissions in the NCP and YRD are reduced, while in the other regions, the emissions of most cities are increased. The changes in $PPM_{2.5}$ emission are similar to SO_2. Compared with the prior emission, the posterior $PPM_{2.5}$ emissions are decreased over central China, SCB and YRD, while the ones in southern and northern China are increased, especially in Shanxi, Shaanxi, Gansu and southern Hebei province. Overall, the relative increase is 95%. For PMC, the posterior emissions are increased over the whole mainland China, with national mean relative increase exceeding 1000%. Larger emission increments mainly occur in the areas where have significant anthropogenic emissions of CO and $PPM_{2.5}$, indicating that the large underestimations of PMC emissions in the prior inventory may be mainly attributed to the underestimations of anthropogenic activities. In addition, the absence of natural dust is another reason, as the wind-blown dust scheme was not applied in this study. Overall, PM10 emissions (PPM2.5+PMC) increased by 318%. If we assume that all the increment in PM_{10} emissions is all from natural dust, that means the contribution of natural dust accounts for 75% of total PM_{10} emissions, which is consistent with the source apportionment of PM_{10} of 75% in Changsha in Central China (Li et al., 2010). Large PMC emission increment are also found in Ma et al (2019).

Detailed estimation of posterior emissions and relative changes compared to prior emissions in each province and the whole mainland China is given in Table S1. The evaluation results for July show that the emission uncertainty can still be significantly

818   reduced, and the performance of the system in July is comparable to that in December

819   (Table S2). Additionally, the seasonal variation of emissions can be well reflected

820   (Figures S4 and S5), which means that our system can perform well at different times

821   of the year. Note that the differences, excluding PMC, between the prior and posterior

822   emissions mainly reflect the deficiencies of the prior emissions because the times of the

823   prior emissions and the observations are completely consistent in this study.
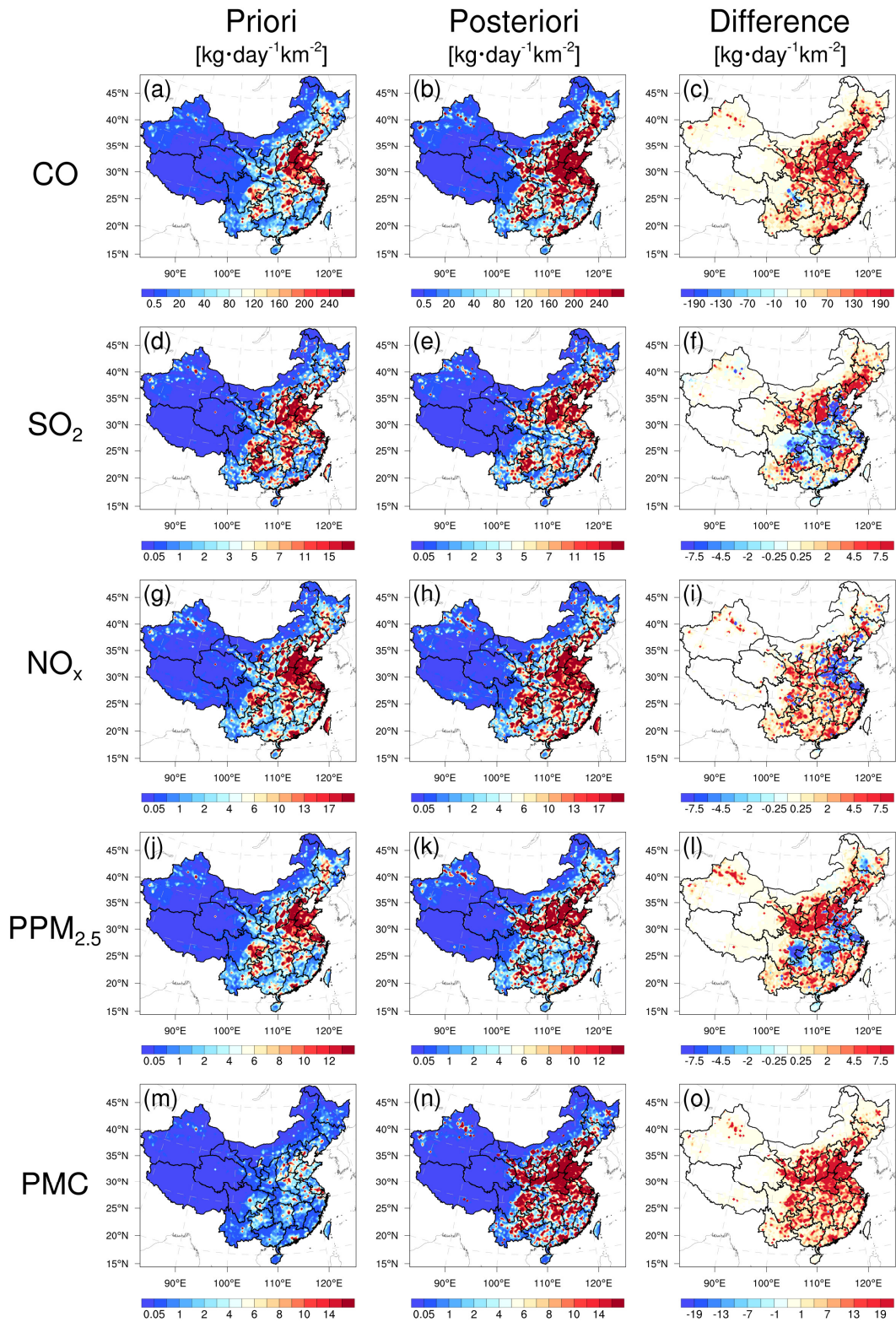
824

825 **Figure 12**. Spatial distribution of the time-averaged prior emissions (left column, MEIC

826 2016), posterior emissions (middle column), and differences (right column, posterior

827 minus prior).

4.3 Sensitivity tests

4.3.1 Impact of prior inventories

Various prior inventories have great differences in space allocation and emission magnitude. Inversion results can be sensitive to a priori emissions if the observation is insufficient (Gurney et al., 2004; He et al., 2018). MEIC 2012 is used as an alternative a priori in EMS2 to investigate the impact of different prior emissions on the posteriori. Figure 13 shows the time series of the relative differences in daily posterior emissions of the five species between the EMDA (base) and EMS2 experiments. Overall, the differences between the two posterior emissions gradually decrease over time. At the beginning, the differences in the CO, SO_2, NO_x, $PPM_{2.5}$ and PMC between the two inventories (i.e., MEIC 2012 vs MEIC 2016) are 17.5%, 114.5%, 30.8%, 46.0% and 72.0%, respectively, while during the last ten days, the differences of the two posterior emissions have decreased to 2.5%, 4.5%, 4.5%, -8.9% and 3.0%, respectively. In addition, it also could be found that the species that has larger emission differences at the beginning take a longer time (namely more DA steps) to achieve convergence. The quick convergence of PMC emission is attributed to the large prior uncertainty of 100% used in the first 3 DA windows. Different from the other species, there are significant negative deviations of $PPM_{2.5}$ emissions between the two experiments. That may be due to the positive deviations in the precursors of $PM_{2.5}$ (i.e., SO_2 and NO_x), which will lead to a larger amount of secondary production. To balance the total $PM_{2.5}$ concentration, the $PPM_{2.5}$ emissions will be reduced. We compare the $PM_{2.5}$ concentrations simulated by the two optimized inventories and find that they are almost the same (Figure S6). Overall, this indicates that the observation in China is sufficient in inferring the emissions, and our system is rather robust. Meanwhile, it also suggests that the monthly posterior emissions shown in Sect. 4.2 are still underestimated to a certain extent.
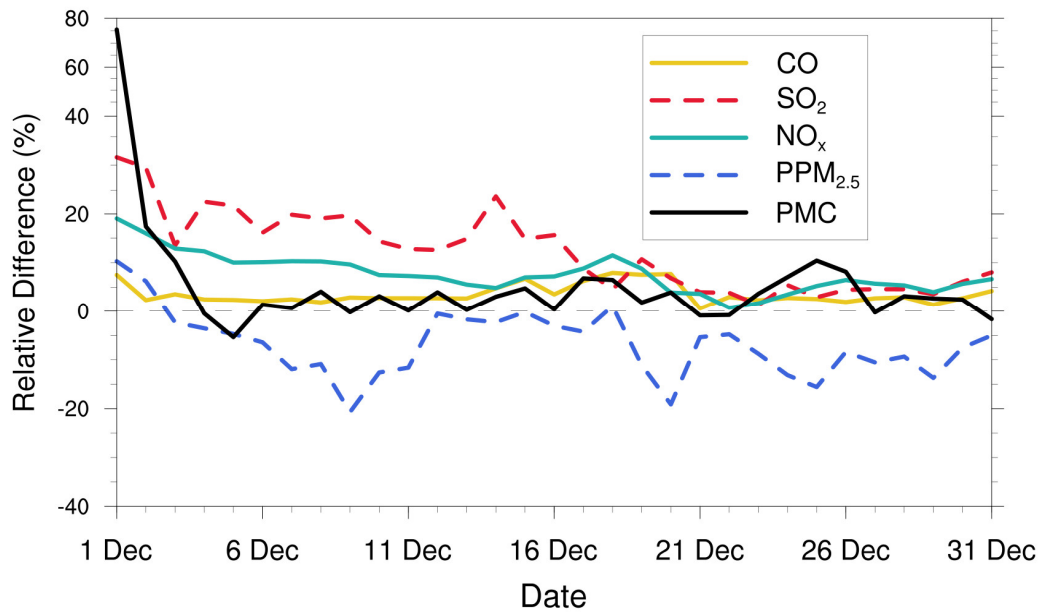
Figure 13. Relative differences in CO, SO$_2$, NO$_x$, PPM$_{2.5}$ and PMC emissions (%, the ratio of absolute difference to EMDA) between the EMDA and EMS2 experiments.

4.3.2 Impact of prior uncertainties settings

The uncertainty of prior emissions determines how closely the analysis is weighted toward the background and observation, but information about prior uncertainties is generally not readily available. To evaluate the possible influence of prior uncertainties on the optimized emissions, we increased/reduced the uncertainties after 3 days of cycling, namely starting at 0000 UTC, 3 December, by 25% and 50 % in EMS3 (-50%), EMS4 (-25%), EMS5 (+25%) and EMS6 (+50%), respectively. Table 7 summarizes the emission changes with different prior uncertainties settings in EMS3-6 experiments. To better understand the response of the system to the emission uncertainty settings, Figure 14 shows the time series of SO$_2$ emission changes, the Chi-square statistics and the RMSEs of simulated SO$_2$ with emissions updated in the EMDA and EMS3-6 experiments over the YRD and NCP (Figure 2). Compared with the EMDA, when the uncertainties are decreased (increased), the emissions of the 5 species decrease (increase) accordingly. That is because the posterior emissions of the 5 species are larger than the prior emissions, and as shown in Figure 14a-d, larger uncertainty will

873 lead to a faster convergence, resulting in larger posterior emissions. It also could be

874 found from Figure 14 that a faster convergence will indeed reduce the RMSE of the

875 simulated concentration with the posterior emissions in the early stage of the

876 experiment, but in the later stage of the experiment, there are no significant differences

877 for the RMSE and Chi-square statistics among the different experiments. However, the

878 day-to-day changes in emissions can also cause slight fluctuations. In addition, it shows

879 that when greater uncertainties are set, the day-to-day changes in emissions are also

880 more drastic, resulting in a larger RMSE as shown in NCP. Moreover, those significant

881 day-to-day variations of estimated emissions may not be in line with the actual situation.

882 Due to the spatial-temporal inhomogeneity of emissions, the differences of Chi-square

883 statistics between the YRD and NCP show that it may be necessary to apply different a

884 priori uncertainties according to different regions (Chen et al., 2019). Therefore, when

885 using an EnKF system for emission estimation, we have to be very careful about the

886 setting of these errors. Overall, the uncertainties chosen in EMDA aim to minimize the

887 deviation of the concentration fields and maintain the stability of inversion.

888 **Table 7**. Relative differences in CO, SO_2, NO_x, $PPM_{2.5}$ and PMC emissions (%, the

889 ratio of absolute difference to EMDA) between the EMDA and EMS3-6 experiments.

Species	EMS3	EMS4	EMS5	EMS6
CO	-8.6	-4	3	5.2
SO_2	-14	-5.7	3.6	6.8
NO_x	-6.5	-3	2.8	4.5
$PPM_{2.5}$	-16.5	-7.8	4.6	8.7
PMC	-18.5	-8.2	7.3	13.1

890

891
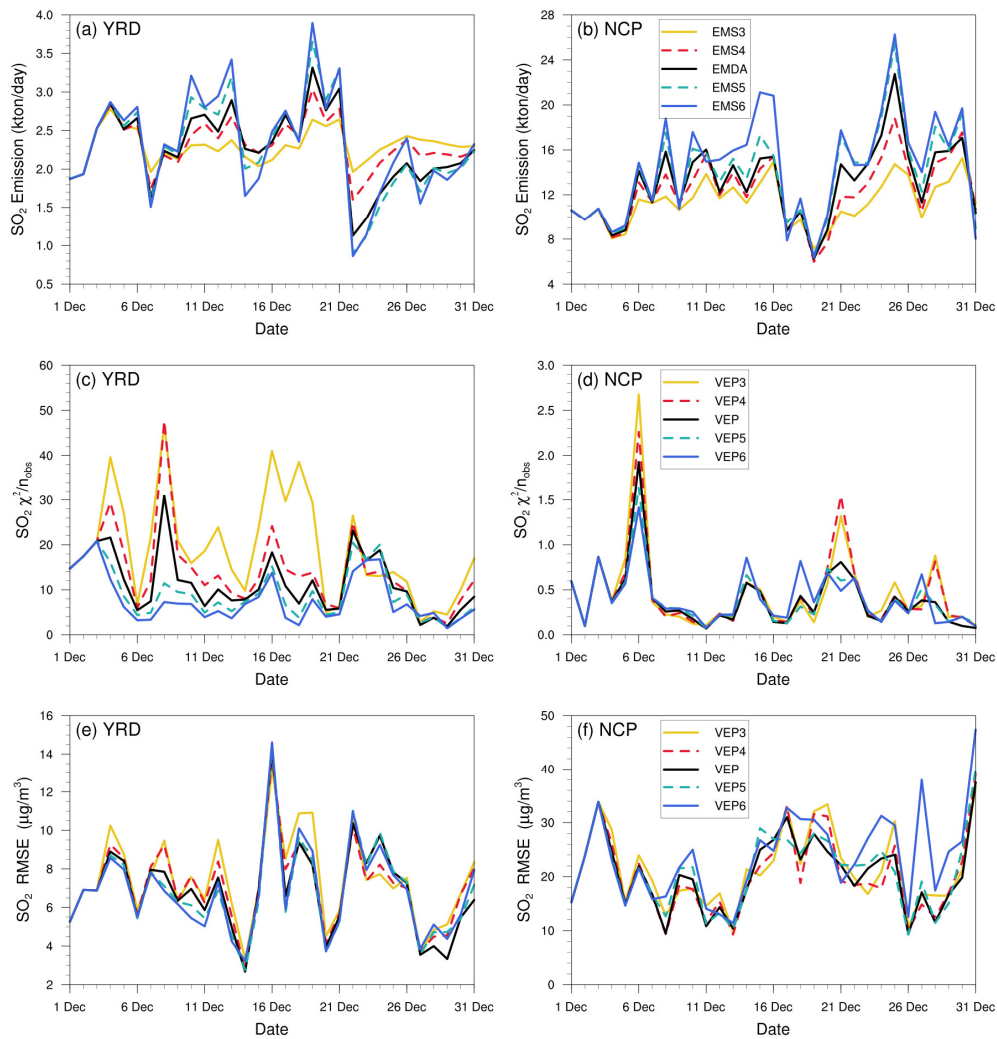
Figure 14. Time-series of SO_2 emission changes, the Chi-square statistics and the RMSE of simulated SO_2 with updated SO_2 emissions in the EMDA and EMS3-6 experiments over the Yangtze River Delta (YRD) and North China Plain (NCP).

4.3.3 Impact of observation error settings

Another factor that determines the relative weights of the observation and background in the analysis is observation errors. A proper estimate of the observation error is also important in regard to the filter performance, but observation errors are not provided with the dataset. The observation error is usually set to a fixed value (Ma et al., 2019), a specific proportion of the observation value (Tang et al., 2013) or the value calculated by combining measurement error with representative error as used in this study. Generally, the performance of the data assimilation is quite sensitive to the specification

of observation error (Tang et al., 2013). To evaluate the influence of observation error on the optimized emissions, a sensitivity experiment (EMS7) with doubled observation error was conducted. Overall, the spatial distribution of emissions after optimization is almost the same as that of the EMDA experiment, but the increment is lower (Figure S7), resulting in a weaker estimate of the national total emission for each species. That is because that the observation error becomes large, the system will be more convinced of the prior emission and reduce the effect of observation information. Figure 15 shows the time series of simulated and observed daily concentrations and their RMSEs verified against the assimilated sites. The simulations in VEP7 usually perform worse, with larger biases and RMSEs than those of VEP (Figures S8 and S9), especially in most of western and southern China where posterior emissions are still significantly underestimated. These results usually correspond to sluggish emission changes and large Chi-square statistics (Figure S10), suggesting that too large observation error may substantially impact the estimated emissions.

917
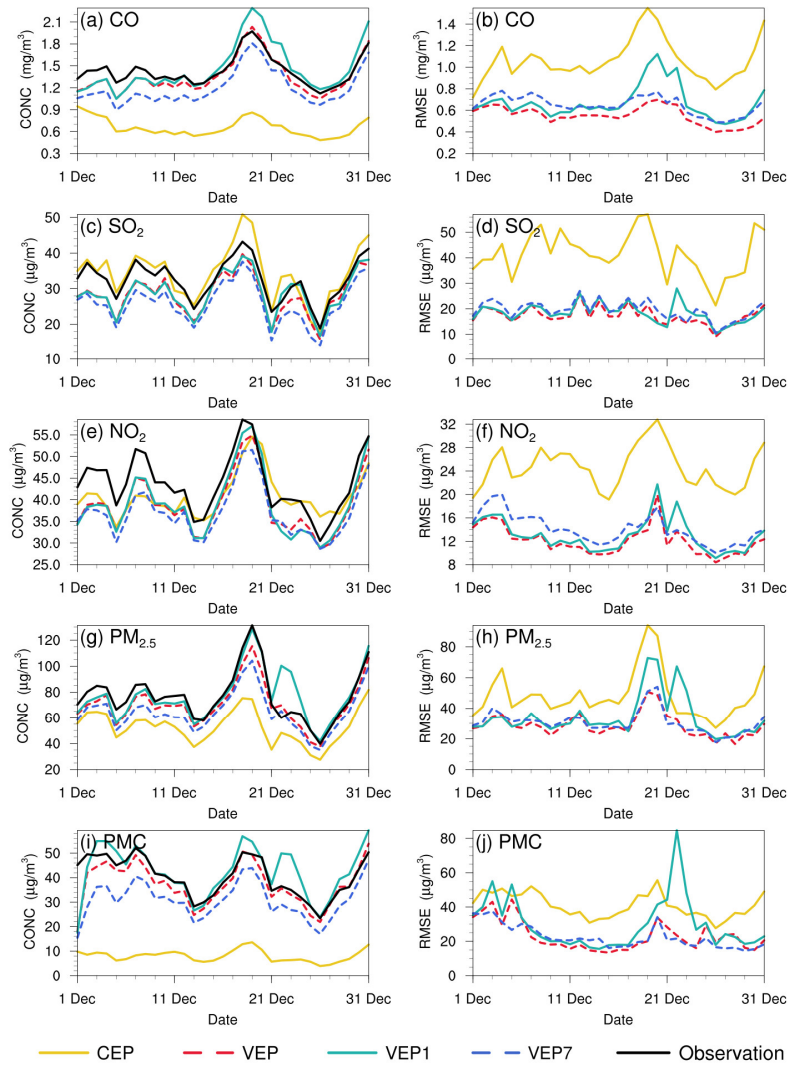
Figure 15. Time series of the daily concentrations (CONC, left) and root mean square error (RMSE, right) obtained from CEP, VEP, VEP1, and VEP7. The simulations were verified against the assimilated sites.

4.3.4 Impact of the IC optimization of the first window

Many studies have shown that there would be large emission discrepancies resulting from the IC errors (Jiang et al., 2013a; Miyazaki et al., 2017; Tang et al., 2013), which means that if the IC is not optimized, the errors of concentrations would be compensated through the adjustment of emissions. To evaluate the impact of the IC optimization of the first window on the emission inversions, the EMS8 experiment without the IA step was conducted. Figure 16 shows the time series of the relative differences in daily

928 posterior emissions of the five species between the EMDA and EMS8 experiments. It

929 can be found that the optimization of IC has great impact on the emission inversions of

930 long-lived species (i.e., CO). The overall difference in the inverted CO emissions

931 between the two experiments is about 5.3%, and in the first few windows, the maximum

932 difference can reach 26.1%. For the short-lived species, the IC optimization has little

933 impact on the emission, for example, the averaged emission differences of SO_2, NO_x

934 and PMC in the two experiments are 0.3%, 0.3% and 0.9%, respectively. For PPM2.5,

935 it is affected not only by the primary emission, but also by the complex chemistry of its

936 precursors. Therefore, the difference between the two experiments fluctuates at a

937 certain extent, with overall difference of 2%. It is worth noting that with the gradual

938 disappearance of the benefit of IC assimilation, the two experiments can reach a unified

939 state after some windows. For CO, the impact of IA on emission inversion lasts about

940 half a month. These results indicate that removing the bias of IC of the first DA window

941 is essential for subsequent inverse analysis (Jiang et al., 2017).
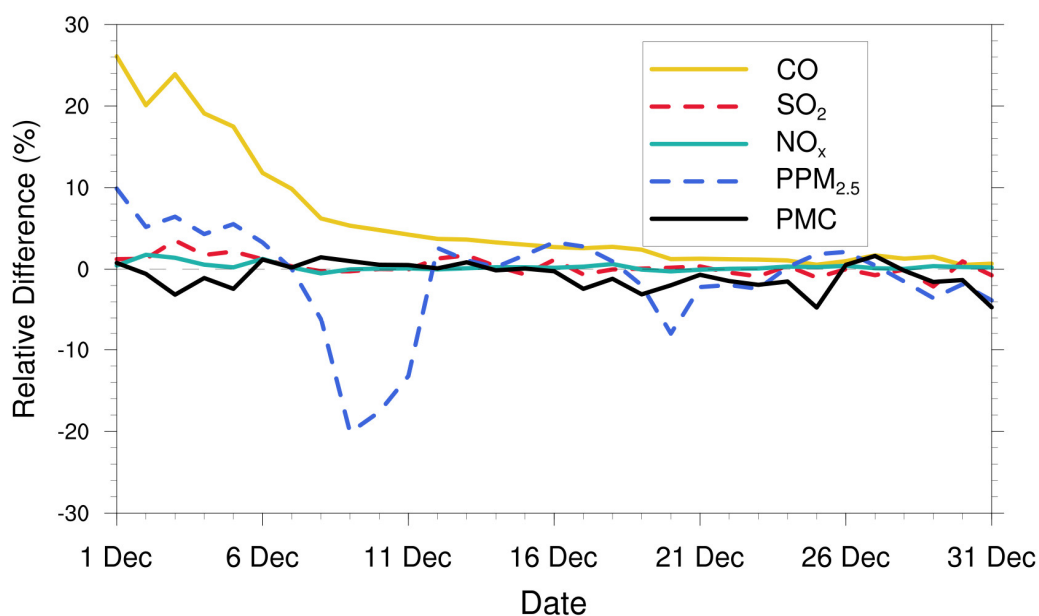
942

943 **Figure 16**. Relative differences in CO, SO2, NOx, PPM2.5 and PMC emissions (%, the

944 ratio of absolute difference to EMDA) between the EMDA and EMS8.

4.3.5 The advantages of "two-step" scheme

Adjusting the ICs and emissions simultaneously (i.e., "one-step" scheme) has been applied to constrain prior emissions in many previous studies (Evensen, 2009; Kong et al., 2019a). To investigate the impact of different methods on the optimized emissions, a sensitivity test (EMS1) was performed, in which the initial fields of each DA window were optimized using the 3DVAR algorithm directly. Compared with our "two-step" method (EMDA), the posterior emissions of EMS1 are increased by 7%, 1.4%, 0.6%, 22.2%, and 17.2% for CO, SO_2, NO_x, $PM_{2.5}$ and PMC, respectively. Overall, there is no significant difference between the two methods for NOx and SO2, but for CO, it can be clearly seen that the difference increases with the inversion (Figure S11). As mentioned previously, in the "two-step" scheme, the unresolved posterior emission error will be fed back to the initial field of the next window through sufficient mixed simulation within one day for timely optimization. Meanwhile, the system always maintains the mass balance of pollutants. In this way, the system updates emissions more consistently and stably. If the emission in one window is overestimated, in this way, it could be compensated in the next window with lower estimates. In contrast, when initial fields assimilating with observations simultaneously at each window, the overestimation will not be corrected and will accumulate to the end. We also evaluate the posterior emissions of EMS1 using the same method as shown in Sect. 4.1.3. Overall, compared to the base experiment (EMDA), the performance of EMS1 is significantly worse, with RMSEs of CO, SO_2, NO_2, $PM_{2.5}$ and PMC increasing from 0.56 mg m^{-3}, 17.7, 12.3, 29.6, and 24.6 μg m^{-3} to 0.69 mg m^{-3}, 18.8, 13.3, 36.8, and 33.3 μg m^{-3}, respectively (Figure 15). Additionally, it can be seen from the figure that the results of the two experiments are relatively close at the beginning and during the heavy pollution period (16-21 December). However, after that, the simulated results with "one-step" inversion emissions are significantly higher than the observations, and these large biases continue until the end. The results verified against the independent sites also show a similar situation (Figure S8). The reason may be that during the period of heavy pollution, the WRF-CMAQ (off-line model) does not consider the feedback process of meteorology

and chemistry, resulting in low simulations. Therefore, the system will compensate for the underestimated concentrations caused by the model error through more emissions, resulting in the overestimation of emissions. The accumulation of emission error in each independent window further leads to the overestimation of concentration after the end of high pollution, especially for species with a long lifetime (e.g., CO). On the contrary, this overestimation will be corrected quickly in the subsequent inversion using the "two-step" inversion scheme in this study (Figure S11), so as to ensure the stability of the system. Additionally, the other "one-step" experiment, taking MEIC 2012 as prior emissions, was conducted. However, the relative differences (Figure S12) in posterior emissions between this experiment and the EMS1 did not converge like that between EMDA and EMS2 with "two-step" scheme (Figure 13), which further demonstrates the advantages of the "two-step" scheme. It should be noted that the model performance depends on many factors but does not affect the advantage of the "two-step" scheme.

4.4 Discussion

Optimal state estimation using an EnKF relies on the assumption of unbiased Gaussian prior error, which is not guaranteed in such highly nonlinear and large biases systems In this study, some pollutants (e.g., CO, PMC) have very large simulated biases, thus if a small uncertainty is adopted, the emission bias cannot been fully reduced, while if a very large uncertainty is adopted, then the degree of freedom of adjustment is too large, and the inverted daily emissions will fluctuate abnormally. Therefore, we only set a larger prior uncertainty in the first three windows, adopted a moderate uncertainty in the following windows, and used a "two-step" inversion scheme and cyclic iteration to gradually correct the emission errors. Figure 10(a) shows the time series of the relative differences between the prior and posterior emissions in each window. There are the relatively large adjustments for the emissions in the first three windows, especially for PMC, but the adjustment ranges of the five species after the first 3 windows are basically within the uncertainty range (e.g., $\pm25\%$), indicating that with this scheme, the EnKF method used in this system still has a good performance in emission inversion.

The model-data mismatch error not only comes from the emissions, but also from the inherent model errors arising from model structure, discretization, parameterizations and the biases in the simulated meteorological fields. Neglecting model errors would attribute all uncertainties to emissions, and lead to considerable biases in the estimated emissions. In the version of CMAQ model used in this study, there is no heterogeneous reactions (Quan et al., 2015; Wang et al., 2017), the parameterization scheme for the formation of secondary organic aerosol (SOA) is imperfect (Carlton et al., 2008; Jiang et al., 2012; Yang et al., 2019), no feedback between chemistry and meteorology is considered, and we used an idea profile for chemical lateral boundary conditions. All of the above problems can lead to underestimated concentrations of pollutants, which in turn require more emissions to compensate, leading to overestimations in emissions. In addition, previous studies have shown that the emission of ammonia in the MEIC inventory was underestimated (Kong et al., 2019b; Paulot et al., 2014; Zhang et al., 2018). Due to lack of ammonia observations, our system does not include emission estimates of ammonia, which means that the concentration of ammonium aerosol was underestimated in this system, also resulting in an overestimation in the $PPM_{2.5}$ emission. Wind-blown dust was also not simulated here, thus the PMC emission inverted in this system do not only come from anthropogenic activities, but also from natural sources. Although some of these shortcomings could be solved in the future by updating the CTM model, there will still be errors in each parameterization and each process. Generally, parameter estimation method was used to reduce the model errors, in which, some uncertain parameters were included in the augmented state vector and were optimized synchronously based on the available observations (Brandhorst et al., 2017; Evensen, 2009). However, it is still quite difficult to identify the key uncertain parameters of different species in different models, which generally comes not only from the complex atmospheric chemical model, but also from hundreds of model inputs (Tang et al., 2013). Another method is bias correction, which treats the model error as a bias term, and includes it in the augmented state vector (Brandhorst et al., 2017; De Lannoy et al., 2007; Keppenne et al., 2005). In addition, the weak-constraint 4D-Var

method can also be used to reduce the model errors, which adds a correction term in the model integration to account for the different sources of model error (Sasaki, 1970). Although reliable diagnosis of model error is still a challenge at present (Laloyaux et al., 2020), it should be considered in an assimilation system. We will consider model errors in our system in the future to obtain better emission estimates.

Independent variable localization was adopted to avoid potential spurious correlations across different species in this study. However, the transmission scales for different species in different regions are still different, and a more accurate localization range could be obtained through backward trajectory analysis. Although Hamer et al. (2015) successfully used O_3 observations to estimate NOx and VOC emissions within the 4D-var framework within an idealised model, O_3 observations are not assimilated to improve NO_x and VOC emissions using cross-species information due to the strong nonlinear effects within the O_3-NO_x-VOC relationship (Wang et al., 2019b), in which the O_3 concentration and NO_x (VOC) emissions are positively correlated in the NO_x (VOC)-limited region and negatively correlated in the VOC (NO_x)-limited region (Tang et al., 2011). This work will be followed up by an ongoing work using available VOC observations. The optimization of the initial fields or emissions of NO_2 may also change the O_3-NO_x-VOC relationship. Assuming that NO_2 is underestimated, the NO_2 concentration increases after assimilation, but the VOC concentration remains unchanged, then in the NOx (VOC)-limited region, the subsequent generation of O_3 will increase (decrease); Conversely, the ozone concentration errors caused by assimilating NO_2 will also affect the subsequent NOx emission inversion. Similarly, the model may not be able to resolve local-scale NO_2 well because of uniform distribution of concentration over the whole grid. Therefore, the model is shifted towards a NO_x (VOC)-limited regime in high (low) pollution regions, which negatively impacts results by perturbing ozone chemistry in unrealistic ways (Inness et al., 2015). To evaluate the influence of O_3-NO_x-VOC relationship change and model resolution on inversion, we also further conducted a nested emission inversion on a densely observed area (the Yangtze River Delta, China) with a grid spacing of 12 km (Feng et al., 2022). The study

period is the same as this study. Results showed that the NOx emissions in the Yangtze River Delta retrieved at two resolutions are almost the same (14.7 kt/day vs. 13.4 kt/day), with a difference of 8.8%, indicating that the emissions can be adjusted effectively by RAPAS. As shown previously, the concentrations after DA are obviously underestimated in western China, indicating that the inverted emissions over these regions still have large uncertainties because of the sparsity of observations that are spatially insufficient for sampling the inhomogeneity of emissions. Therefore, further investigations with joint assimilation of multisource observations (e.g., satellite) are also underway.

When comparing the performances of the "two-step" and "one-step" schemes, for the "one-step" scheme, we use a combination assimilation method, namely 3DVAR for the optimizations of initial fields and EnKF for emission inversions in each DA window, which is similar as Jiang et al., (2017), but different from most previous studies (Miyazaki et al., 2017; Tang et al., 2013). Because most previous "one-step" assimilation studies used only one method (i.e., EnKF). This combination method may cause the comparison less than perfect. However, it should be noted that, even using the same method (such as EnKF) to optimize the emission of the current window and the initial field of the next window simultaneously (Peng et al., 2018), the initial field estimation errors will still be mixed in the simulated concentration field, resulting in unreasonable emission compensation in the next window. In "one-step" scheme, the essence is to build a good initial field in the high levels. Schwartz et al. (2014) compared the performances of EnKF and 3DVAR in optimizing initial fields, and found that 3DVAR method can obtain a better initial field than EnKF method. Therefore, we believe that in this comparison, a combinatorial assimilation approach used in the "one-step" scheme is an acceptable approach, and the conclusion is credible, that the "two-step" scheme has better performances than the "one-step" scheme in emission estimates.

NOx is mainly emitted by transportation (Li et al., 2017), which can better reflect the level of economic activities to a certain extent. Weekly emission changes were also explored to verify the performance of the system in depicting emission changes (Figure

S13). Although the "weekend effect" of emissions in China is not significant (Wang et al., 2014; Wang et al., 2015), the posterior NOx emission changes showed a good agreement with the observations. In our previous studies (Feng et al., 2020a; Feng et al., 2020b), the system was successfully applied to optimize NOx and CO emissions, respectively. The inverted emission changes were also in line with the time points of epidemic control. Additionally, the emission changes can well reflect the emission migration from developed regions or urban areas to developing regions or surrounding areas over recent years, which were consistent with the emission control strategies in China. Although the system does not consider the model error, resulting in a certain difference between the posterior emission and the actual emission, the spatiotemporal changes in posterior emissions are relatively reasonable, which can be used to monitor emission changes and make emission regulations.

5 Summary and conclusions

In this study, we developed a Regional multi-Air Pollutant Assimilation System (RAPASv1.0) based on the WRF/CMAQ model, 3DVAR and EnKF algorithm. RAPAS can quantitatively optimize gridded emissions of CO, SO_2, NO_x, $PPM_{2.5}$ and PMC on regional scale by simultaneously assimilating hourly in-situ measurements of CO, SO_2, NO_2, $PM_{2.5}$ and PM_{10}. This system includes two subsystems, namely the IA subsystem and the EI subsystem, which optimizes the chemical ICs, and infers the anthropogenic emissions, respectively.

Taking the 2016 Multi-resolution Emission Inventory for China (MEIC 2016) in December as a priori, the emissions of CO, SO_2, NO_x, $PPM_{2.5}$ and PMC in December 2016 were inferred through assimilating the corresponding nationwide observations over China. The optimized ICs and posterior emissions were examined against the assimilated and independent observations through parallel forward simulation experiments with and without DA. Sensitivity tests are also performed to investigate the impact of different inversion processes, prior emissions, prior uncertainties and observation errors on the emission estimates.

The results show that RAPAS has a good performance in assimilating ground in-situ observations, with the calculated emission uncertainties reduced by 44.4%, 45.0%, 34.3%, 51.8% and 56.1% for CO, SO_2, NO_x, $PPM_{2.5}$ and PMC, respectively. It can also significantly improve the simulations, the RMSEs of the simulated concentrations with posterior emissions decreased by 40.1-56.3%, and the CORRs increased from 0.26-0.66 to 0.69-0.87 for different species. The OSSE experiment shows that the error of posterior CO, SO_2, NO_x, PPM2.5, and PMC could be reduced by 78.4%, 86.1%, 78.8%, 77.6%, and 72.0%, respectively. Overall, compared with the prior emissions (MEIC 2016), the posterior emissions increased by 129%, 20%, 5% and 95% for CO, SO_2, NO_x and $PPM_{2.5}$, respectively. The posterior PMC emissions, which included anthropogenic and natural dust contributions, increased by 1045%. The sensitivity tests with different inversion processes show that the "two-step" scheme in emission inversion outperforms the joint adjustment of ICs and emissions ("one-step" scheme), especially after heavy pollution. The sensitivity tests with different prior inventories show the observation in China is sufficient in inferring the emissions, and our system is less dependent on prior inventories. Additionally, the sensitivity tests with different prior uncertainties indicate that when the posterior emissions are larger than the prior emissions, the emissions decrease/increase with the decreases/increases of uncertainties because of the different convergence rates. These results demonstrate the advantage of the two-step method in emission inversion in that the inversion errors of the last window could be transferred to the current window for further optimization and the robustness of the emissions estimated from RAPAS using the nationwide observations over China. It should be noted that the system usually responds slowly to too small a priori uncertainty or too large observation error, which may result in large errors in the estimated emissions.

In summary, the comprehensive evaluation and sensitivity tests reveal that RAPAS could serve as a useful tool for accurately quantifying the spatial and temporal changes of multi-species emissions at regional scales and near-real time, which will be helpful for the air pollution control in China, and the other regions around the world with dense ground observation networks.

Code and data availability

The codes of RAPAS v1.0 are available at https://doi.org/10.5281/zenodo.5566225. The WRF model code is open-source code and can be obtained from the WRF Model User's Page (https://www2.mmm.ucar.edu/wrf/users, last access: 25 April 2021). The CMAQ model is available through an open license as well (https://www.epa.gov/cmaq , last access: 25 April 2021). The observation and emission data used in this paper are available at https://doi.org/10.5281/zenodo.4718290 (Feng and Jiang, 2021).

Author contribution

SF, FJ, ZW and ZJ developed RAPAS v1.0. SF and FJ designed the research. SF performed model simulations, analyzed data, and prepared the paper with contributions from all co-authors. FJ supervised the model development project and assisted in conceptualization and writing. HW, WH, YS, LZ, YZ, CL, and WJ contributed to the discussion and improvement of the paper.

Competing interests

The authors declare that they have no conflict of interest.

Acknowledgements

This work is supported by the National Key R&D Program of China (Grant No. 2016YFA0600204), the National Natural Science Foundation of China (Grant No. 41907378), and the Nanjing University Innovation and Creative Program for Ph.D. candidate (Grant No. CXCY19-60). We are grateful to the High Performance Computing Center (HPCC) of Nanjing University for doing the numerical calculations in this paper on its blade cluster system, and thank the MEIC team for providing the prior anthropogenic emissions (http://www.meicmodel.org/).

References

Appel, K. W., Pouliot, G. A., Simon, H., Sarwar, G., Pye, H. O. T., Napelenok, S. L., Akhtar, F., and Roselle, S. J.: Evaluation of dust and trace metal estimates from the Community Multiscale Air Quality (CMAQ) model version 5.0, Geoscientific Model Development, 6, 883-899, 10.5194/gmd-6-883-2013, 2013.

Alexe, M., Bergamaschi, P., Segers, A., Detmers, R., Butz, A., Hasekamp, O., Guerlet, S., Parker, R., Boesch, H., Frankenberg, C., Scheepmaker, R. A., Dlugokencky, E., Sweeney, C., Wofsy, S. C., and Kort, E. A.: Inverse modelling of CH4 emissions for 2010-2011 using different satellite retrieval products from GOSAT and SCIAMACHY, Atmospheric Chemistry and Physics, 15, 113-133, 2015.

Barbu, A. L., Segers, A. J., Schaap, M., Heemink, A. W., and Builtjes, P. J. H.: A multi-component data assimilation experiment directed to sulphur dioxide and sulphate over Europe, Atmospheric Environment, 43, 1622-1631, 2009.

Basu, S., Guerlet, S., Butz, A., Houweling, S., Hasekamp, O., Aben, I., Krummel, P., Steele, P., Langenfelds, R., Torn, M., Biraud, S., Stephens, B., Andrews, A., and Worthy, D.: Global CO2 fluxes estimated from GOSAT retrievals of total column CO2, Atmospheric Chemistry and Physics, 13, 8695-8717, 2013.

Bauwens, M., Compernolle, S., Stavrakou, T., Müller, J.-F., van Gent, J., Eskes, H., Levelt, P. F., van der A, R., Veefkind, J. P., Vlietinck, J., Yu, H., and Zehner, C.: Impact of Coronavirus Outbreak on NO2 Pollution Assessed Using TROPOMI and OMI Observations, 47, e2020GL087978, 10.1029/2020gl087978, 2020.

Bierman: Factorization methods for Discrete Sequential estimation, Academic Press, 1977.

Binkowski, F. S. and Roselle, S. J.: Models-3 community multiscale air quality (CMAQ) model aerosol component - 1. Model description, Journal of Geophysical Research-Atmospheres, 108, 10.1029/2001jd001409, 2003.

Brandhorst, N., Erdal, D., and Neuweiler, I.: Soil moisture prediction with the ensemble Kalman filter: Handling uncertainty of soil hydraulic parameters, Advances in Water Resources, 110, 360-370, 2017.

Bruhwiler, L. M. P., Michalak, A. M., Peters, W., Baker, D. F., and Tans, P.: An improved Kalman Smoother for atmospheric inversions, Atmos. Chem. Phys., 5, 2691-2702, 10.5194/acp-5-2691-2005, 2005.

Carlton, A. G., Turpin, B. J., Altieri, K. E., Seitzinger, S. P., Mathur, R., Roselle, S. J., and Weber, R. J.: CMAQ Model Performance Enhanced When In-Cloud Secondary Organic Aerosol is Included: Comparisons of Organic Carbon Predictions with Measurements, Environmental Science & Technology, 42, 8798-8802, 2008

Chen, D., Liu, Z., Ban, J., and Chen, M.: The 2015 and 2016 wintertime air pollution in China: SO2 emission changes derived from a WRF-Chem/EnKF coupled data assimilation system, Atmospheric Chemistry and Physics, 19, 8619-8650, 10.5194/acp-19-8619-2019, 2019.

Chen, D., Liu, Z., Fast, J., and Ban, J.: Simulations of sulfate-nitrate-ammonium (SNA) aerosols during the extreme haze events over northern China in October 2014, Atmospheric Chemistry and Physics, 16, 10707-10724, 10.5194/acp-16-10707-2016, 2016.

1213 Chevallier, F., Bréon, F.-M., and Rayner, P. J.: Contribution of the Orbiting Carbon Observatory to
1214   the estimation of CO2 sources and sinks: Theoretical study in a variational data assimilation
1215   framework, 112, 10.1029/2006JD007375, 2007.

1216 Clements, A. L., Fraser, M. P., Upadhyay, N., Herckes, P., Sundblom, M., Lantz, J., and Solomon,
1217   P. A.: Chemical characterization of coarse particulate matter in the Desert Southwest - Pinal
1218   County Arizona, USA, Atmospheric Pollution Research, 5, 52-61, 10.5094/apr.2014.007, 2014.

1219 Clements, N., Hannigan, M. P., Miller, S. L., Peel, J. L., and Milford, J. B.: Comparisons of urban
1220   and rural PM10-2.5 and PM2.5 mass concentrations and semi-volatile fractions in northeastern
1221   Colorado, Atmospheric Chemistry and Physics, 16, 7469-7484, 10.5194/acp-16-7469-2016, 2016.

1222 Daley, R.: Atmospheric Data Assimilation (gtSpecial IssueltData Assimilation in Meteology and
1223   Oceanography: Theory and Practice), Journal of the Meteorological Society of Japan. Ser. II, 75,
1224   319-329, 1997.

1225 Derber, J. C.: A VARIATIONAL CONTINUOUS ASSIMILATION TECHNIQUE, Monthly
1226   Weather Review, 117, 2437-2446, 1989.

1227 de Foy, B., Lu, Z., Streets, D. G., Lamsal, L. N., and Duncan, B. N.: Estimates of power plant NOx
1228   emissions and lifetimes from OMI NO2 satellite retrievals, Atmospheric Environment, 116, 1-11,
1229   10.1016/j.atmosenv.2015.05.056, 2015.

1230 De Lannoy, G. J. M., Houser, P. R., Pauwels, V. R. N., and Verhoest, N. E. C.: State and bias
1231   estimation for soil moisture profiles by an ensemble Kalman filter: Effect of assimilation depth
1232   and frequency, 43, 2007.

1233 Ding, J., van der A, R. J., Mijling, B., Levelt, P. F., and Hao, N.: NOx emission estimates during the
1234   2014 Youth Olympic Games in Nanjing, Atmospheric Chemistry and Physics, 15, 9399-9412,
1235   10.5194/acp-15-9399-2015, 2015.

1236 Elbern, H., Strunk, A., Schmidt, H., and Talagrand, O.: Emission rate and chemical state estimation
1237   by 4-dimensional variational inversion, Atmospheric Chemistry and Physics, 7, 3749-3769,
1238   10.5194/acp-7-3749-2007, 2007.

1239 Evensen, G.: The Ensemble Kalman Filter for Combined State and Parameter Estimation MONTE
1240   CARLO TECHNIQUES FOR DATA ASSIMILATION IN LARGE SYSTEMS, Ieee Control
1241   Systems Magazine, 29, 83-104, 10.1109/mcs.2009.932223, 2009.

1242 Feng, S., Jiang, F., Jiang, Z., Wang, H., Cai, Z., and Zhang, L.: Impact of 3DVAR assimilation of
1243   surface PM2.5 observations on PM2.5 forecasts over China during wintertime, Atmospheric
1244   Environment, 187, 34-49, 10.1016/j.atmosenv.2018.05.049, 2018.

1245 Feng, S., Jiang, F., Wang, H., Shen, Y., Zheng, Y., Zhang, L., Lou, C., and Ju, W.: Anthropogenic
1246   emissions estimated using surface observations and their impacts on PM2.5 source apportionment
1247   over the Yangtze River Delta, China, Science of The Total Environment, 828, 154522, 2022

1248 Feng, S., Jiang, F., Wu, Z., Wang, H., Ju, W., and Wang, H.: CO Emissions Inferred From Surface
1249   CO Observations Over China in December 2013 and 2017, Journal of Geophysical Research-
1250   Atmospheres, 125, 10.1029/2019jd031808, 2020a.

1251 Feng, S., Jiang, F., Wang, H., Wang, H., Ju, W., Shen, Y., Zheng, Y., Wu, Z., and Ding, A.: NOx
1252   Emission Changes Over China During the COVID-19 Epidemic Inferred From Surface NO2
1253   Observations, Geophysical Research Letters, 47, 10.1029/2020gl090080, 2020b.

1254 Feng, S. and Jiang, F.: Anthropogenic air pollutant emissions over China inferred by Regional multi-

Air Pollutant Assimilation System (RAPAS v1.0), Zenodo, 10.5281/zenodo.4718290, 2021.

Gaspari, G. and Cohn, S. E.: Construction of correlation functions in two and three dimensions, Quarterly Journal of the Royal Meteorological Society, 125, 723-757, 10.1256/smsqj.55416, 1999.

Guenther, A. B., Jiang, X., Heald, C. L., Sakulyanontvittaya, T., Duhl, T., Emmons, L. K., and Wang, X.: The Model of Emissions of Gases and Aerosols from Nature version 2.1 (MEGAN2.1): an extended and updated framework for modeling biogenic emissions, Geoscientific Model Development, 5, 1471-1492, 10.5194/gmd-5-1471-2012, 2012.

Gurney, K. R., Law, R. M., Denning, A. S., Rayner, P. J., Pak, B. C., Baker, D., Bousquet, P., Bruhwiler, L., Chen, Y. H., Ciais, P., Fung, I. Y., Heimann, M., John, J., Maki, T., Maksyutov, S., Peylin, P., Prather, M., and Taguchi, S.: Transcom 3 inversion intercomparison: Model mean results for the estimation of seasonal carbon sources and sinks, Global Biogeochemical Cycles, 18, 10.1029/2003gb002111, 2004.

He, W., van der Velde, I. R., Andrews, A. E., Sweeney, C., Miller, J., Tans, P., van der Laan-Luijkx, I. T., Nehrkorn, T., Mountain, M., Ju, W., Peters, W., and Chen, H.: CTDAS-Lagrange v1.0: a high-resolution data assimilation system for regional carbon dioxide observations, Geoscientific Model Development, 11, 3515-3536, 10.5194/gmd-11-3515-2018, 2018.

Hinds, W.C.: Aerosol Technology: Properties, Behavior, and Measurement of Airborne Particles. New York: John Wiley, 1982.

Houtekamer, P. L. and Mitchell, H. L.: A sequential ensemble Kalman filter for atmospheric data assimilation, Monthly Weather Review, 129, 123-137, 10.1175/1520-0493(2001)129<0123:asekff>2.0.co;2, 2001.

Houtekamer, P. L. and Zhang, F.: Review of the Ensemble Kalman Filter for Atmospheric Data Assimilation, Monthly Weather Review, 144, 4489-4532, 10.1175/mwr-d-15-0440.1, 2016.

Inness, A., Blechschmidt, A. M., Bouarar, I., Chabrillat, S., Crepulja, M., Engelen, R. J., Eskes, H., Flemming, J., Gaudel, A., Hendrick, F., Huijnen, V., Jones, L., Kapsomenakis, J., Katragkou, E., Keppens, A., Langerock, B., de Maziere, M., Melas, D., Parrington, M., Peuch, V. H., Razinger, M., Richter, A., Schultz, M. G., Suttie, M., Thouret, V., Vrekoussis, M., Wagner, A., and Zerefos, C.: Data assimilation of satellite-retrieved ozone, carbon monoxide and nitrogen dioxide with ECMWF's Composition-IFS, Atmospheric Chemistry and Physics, 15, 5275-5303, 2015.

Jiang, F., Liu, Q., Huang, X., Wang, T., Zhuang, B., and Xie, M.: Regional modeling of secondary organic aerosol over China using WRF/Chem, Journal of Aerosol Science, 43, 57-73, 10.1016/j.jaerosci.2011.09.003, 2012a.

Jiang, F., Zhou, P., Liu, Q., Wang, T., Zhuang, B., and Wang, X.: Modeling tropospheric ozone formation over East China in springtime, Journal of Atmospheric Chemistry, 69, 303-319, 10.1007/s10874-012-9244-3, 2012b.

Jiang, F., Wang, H. M., Chen, J. M., Machida, T., Zhou, L. X., Ju, W. M., Matsueda, H., and Sawa, Y.: Carbon balance of China constrained by CONTRAIL aircraft CO_2 measurements, Atmospheric Chemistry and Physics, 14, 10133-10144, 10.5194/acp-14-10133-2014, 2014.

Jiang, F., Wang, H., Chen, J. M., Ju, W., Tian, X., Feng, S., Li, G., Chen, Z., Zhang, S., Lu, X., Liu, J., Wang, H., Wang, J., He, W., and Wu, M.: Regional CO_2 fluxes from 2010 to 2015 inferred from GOSAT XCO2 retrievals using a new version of the Global Carbon Assimilation System, Atmos. Chem. Phys., 21, 1963-1985, 10.5194/acp-21-1963-2021, 2021.

Jiang, W., Smyth, S., Giroux, E., Roth, H., and Yin, D.: Differences between CMAQ fine mode particle and PM2.5 concentrations and their impact on model performance evaluation in the lower Fraser valley, Atmospheric Environment, 40, 4973-4985, 10.1016/j.atmosenv.2005.10.069, 2006.

Jiang, Z., Jones, D. B. A., Worden, H. M., Deeter, M. N., Henze, D. K., Worden, J., Bowman, K. W., Brenninkmeijer, C. A. M., and Schuck, T. J.: Impact of model errors in convective transport on CO source estimates inferred from MOPITT CO retrievals, Journal Of Geophysical Research-Atmospheres, 118, 2073-2083, 2013a.

Jiang, Z., Liu, Z., Wang, T., Schwartz, C. S., Lin, H.-C., and Jiang, F.: Probing into the impact of 3DVAR assimilation of surface PM10 observations over China using process analysis, Journal of Geophysical Research: Atmospheres, 118, 6738-6749, 10.1002/jgrd.50495, 2013b.

Jiang, Z., Worden, J. R., Worden, H., Deeter, M., Jones, D. B. A., Arellano, A. F., and Henze, D. K.: A 15-year record of CO emissions constrained by MOPITT CO observations, Atmospheric Chemistry And Physics, 17, 4565-4583, 10.5194/acp-17-4565-2017, 2017.

Jin, J., Lin, H. X., Heemink, A., and Segers, A.: Spatially varying parameter estimation for dust emissions using reduced-tangent-linearization 4DVar, Atmospheric Environment, 187, 358-373, 10.1016/j.atmosenv.2018.05.060, 2018.

Kahnert, M.: Variational data analysis of aerosol species in a regional CTM: background error covariance constraint and aerosol optical observation operators, Tellus B, 60, 2008.

Kang, J.-S., Kalnay, E., Miyoshi, T., Liu, J., and Fung, I.: Estimation of surface carbon fluxes with an advanced data assimilation methodology, 117, 10.1029/2012JD018259, 2012.

Keppenne, C. L., Rienecker, M. M., Kurkowski, N. P., and Adamec, D. A.: Ensemble Kalman filter assimilation of temperature and altimeter data with bias correction and application to seasonal prediction, Nonlin. Processes Geophys., 12, 491-503, 2005.

Kleist, D. T., Parrish, D. F., Derber, J. C., Treadon, R., Wu, W.-S., and Lord, S.: Introduction of the GSI into the NCEP Global Data Assimilation System, Weather and Forecasting, 24, 1691-1705, 10.1175/2009waf2222201.1, 2009.

Kong, L., Tang, X., Zhu, J., Wang, Z., Pan, Y., Wu, H., Wu, L., Wu, Q., He, Y., Tian, S., Xie, Y., Liu, Z., Sui, W., Han, L., and Carmichael, G.: Improved Inversion of Monthly Ammonia Emissions in China Based on the Chinese Ammonia Monitoring Network and Ensemble Kalman Filter, Environmental Science & Technology, 53, 12529-12538, 10.1021/acsest.9b02701, 2019a.

Kong, L., Tang, X., Zhu, J., Wang, Z., Fu, J. S., Wang, X., Itahashi, S., Yamaji, K., Nagashima, T., Lee, H. J., Kim, C. H., Lin, C. Y., Chen, L., Zhang, M., Tao, Z., Li, J., Kajino, M., Liao, H., Sudo, K., Wang, Y., Pan, Y., Tang, G., Li, M., Wu, Q., Ge, B., and Carmichael, G. R.: Evaluation and uncertainty investigation of the NO2, CO and NH3 modeling over China under the framework of MICS-Asia III, Atmos. Chem. Phys. Discuss., 2019, 1-33, 10.5194/acp-2018-1158, 2019b.

Kurokawa, J.-i., Yumimoto, K., Uno, I., and Ohara, T.: Adjoint inverse modeling of NOx emissions over eastern China using satellite observations of NO2 vertical column densities, Atmospheric Environment, 43, 1878-1887, 10.1016/j.atmosenv.2008.12.030, 2009.

Laloyaux, P., Bonavita, M., Chrust, M., and Gürol, S.: Exploring the potential and limitations of weak-constraint 4D-Var, Quarterly Journal of the Royal Meteorological Society, 146, 4067-4082, 2020

Li, J.-d., Deng, Q.-h., Lu, C., and Huang, B.-l.: Chemical compositions and source apportionment

of atmospheric PM10 in suburban area of Changsha, China, Journal of Central South University of Technology, 17, 509-515, 2010.

Li, M., Zhang, Q., Kurokawa, J.-i., Woo, J.-H., He, K., Lu, Z., Ohara, T., Song, Y., Streets, D. G., Carmichael, G. R., Cheng, Y., Hong, C., Huo, H., Jiang, X., Kang, S., Liu, F., Su, H., and Zheng, B.: MIX: a mosaic Asian anthropogenic emission inventory under the international collaboration framework of the MICS-Asia and HTAP, Atmospheric Chemistry and Physics, 17, 935-963, 10.5194/acp-17-935-2017, 2017.

Liu, Z., Liu, Q., Lin, H.-C., Schwartz, C. S., Lee, Y.-H., and Wang, T.: Three-dimensional variational assimilation of MODIS aerosol optical depth: Implementation and application to a dust storm over East Asia, Journal of Geophysical Research: Atmospheres, 116, n/a-n/a, 10.1029/2011jd016159, 2011.

Lorenc, A. C.: Modelling of error covariances by 4D-Var data assimilation, Quarterly Journal of the Royal Meteorological Society, 129, 3167-3182, 2003.

Hamer, P. D., Bowman, K. W., Henze, D. K., Attie, J. L., and Marecal, V.: The impact of observing characteristics on the ability to predict ozone under varying polluted photochemical regimes, Atmospheric Chemistry and Physics, 15, 10645-10667, 2015.

Ma, C., Wang, T., Mizzi, A. P., Anderson, J. L., Zhuang, B., Xie, M., and Wu, R.: Multiconstituent Data Assimilation With WRF-Chem/DART: Potential for Adjusting Anthropogenic Emissions and Improving Air Quality Forecasts Over Eastern China, 124, 7393-7412, 10.1029/2019jd030421, 2019.

Meirink, J. F., Eskes, H. J., and Goede, A. P. H.: Sensitivity analysis of methane emissions derived from SCIAMACHY observations through inverse modelling, Atmospheric Chemistry and Physics, 6, 1275-1292, 10.5194/acp-6-1275-2006, 2006.

Maybeck: Stochastic Models, Estimation and Control Academic Press, 1979.

Miyazaki, K. and Eskes, H.: Constraints on surface NOx emissions by assimilating satellite observations of multiple species, Geophysical Research Letters, 40, 4745-4750, 10.1002/grl.50894, 2013.

Miyazaki, K., Eskes, H. J., and Sudo, K.: Global NOx emission estimates derived from an assimilation of OMI tropospheric NO2 columns, Atmospheric Chemistry and Physics, 12, 2263-2288, 10.5194/acp-12-2263-2012, 2012a.

Miyazaki, K., Eskes, H. J., Sudo, K., Takigawa, M., van Weele, M., and Boersma, K. F.: Simultaneous assimilation of satellite NO2, O-3, CO, and HNO3 data for the analysis of tropospheric chemical composition and emissions, Atmospheric Chemistry and Physics, 12, 9545-9579, 10.5194/acp-12-9545-2012, 2012b.

Miyazaki, K., Eskes, H., Sudo, K., Boersma, K. F., Bowman, K., and Kanaya, Y.: Decadal changes in global surface NOx emissions from multi-constituent satellite data assimilation, Atmospheric Chemistry and Physics, 17, 807-837, 2017.

Monteil, G., Houweling, S., Butz, A., Guerlet, S., Schepers, D., Hasekamp, O., Frankenberg, C., Scheepmaker, R., Aben, I., and Rockmann, T.: Comparison of CH4 inversions based on 15 months of GOSAT and SCIAMACHY observations, Journal of Geophysical Research-Atmospheres, 118, 11807-11823, 2013.

Nassar, R., Jones, D. B. A., Kulawik, S. S., Worden, J. R., Bowman, K. W., Andres, R.

J., Suntharalingam, P., Chen, J. M., Brenninkmeijer, C. A. M., Schuck, T. J., Conway, T. J., and Worthy, D. E.: Inverse modeling of CO2 sources and sinks using satellite observations of CO2 from TES and surface flask measurements, Atmospheric Chemistry and Physics, 11, 6029-6047, 2011.

Parrish, D. F. and Derber, J. C.: The National Meteorological Center's spectral statistical-interpolation analysis system, Monthly Weather Review, 120, 1747-1763, 10.1175/1520-0493(1992)120<1747:tnmcss>2.0.co;2, 1992.

Paulot, F., Jacob, D. J., Pinder, R. W., Bash, J. O., Travis, K., and Henze, D. K.: Ammonia emissions in the United States, European Union, and China derived by high-resolution inversion of ammonium wet deposition data: Interpretation with a new agricultural emissions inventory (MASAGE_NH3), Journal of Geophysical Research-Atmospheres, 119, 4343-4364, 2014.

Peng, Z., Liu, Z., Chen, D., and Ban, J.: Improving PM$_{2.5}$ forecast over China by the joint adjustment of initial conditions and source emissions with an ensemble Kalman filter, Atmospheric Chemistry and Physics, 17, 4837-4855, 10.5194/acp-17-4837-2017, 2017.

Peng, Z., Lei, L., Liu, Z., Su, J., Ding, A., Ban, J., Chen, D., Kou, X., and Chu, K.: The impact of multi-species surface chemical observation assimilation on air quality forecasts in China, Atmospheric Chemistry and Physics, 18, 10.5194/acp-18-17387-2018, 2018.

Peters, W., Jacobson, A. R., Sweeney, C., Andrews, A. E., Conway, T. J., Masarie, K., Miller, J. B., Bruhwiler, L. M. P., Petron, G., Hirsch, A. I., Worthy, D. E. J., van der Werf, G. R., Randerson, J. T., Wennberg, P. O., Krol, M. C., and Tans, P. P.: An atmospheric perspective on North American carbon dioxide exchange: CarbonTracker, Proceedings of the National Academy of Sciences of the United States of America, 104, 18925-18930, 10.1073/pnas.0708986104, 2007.

Peylin, P., Rayner, P. J., Bousquet, P., Carouge, C., Hourdin, F., Heinrich, P., Ciais, P., and contributors, A.: Daily CO2 flux estimates over Europe from continuous atmospheric measurements: 1, inverse methodology, Atmospheric Chemistry and Physics, 5, 3173-3186, 10.5194/acp-5-3173-2005, 2005.

Purser, R. J., Wu, W. S., Parrish, D. F., and Roberts, N. M.: Numerical aspects of the application of recursive filters to variational statistical analysis. Part I: Spatially homogeneous and isotropic Gaussian covariances, Monthly Weather Review, 131, 1524-1535, 10.1175//1520-0493(2003)131<1524:naotao>2.0.co;2, 2003.

Quan, J., Liu, Q., Li, X., Gao, Y., Jia, X., Sheng, J., Liu, Y., 2015. Effect of heterogeneous aqueous reactions on the secondary formation of inorganic aerosols during haze events. Atmospheric Environment 122, 306-312.

Rabier, F., McNally, A., Andersson, E., Courtier, P., Unden, P., Eyre, J., Hollingsworth, A., and Bouttier, F.: The ECMWF implementation of three-dimensional variational assimilation (3D-Var). II: Structure functions, Quarterly Journal Of the Royal Meteorological Society, 124, 1809-1829, 10.1256/smsqj.55002, 1998.

Reichle, R. H., McLaughlin, D. B., and Entekhabi, D.: Hydrologic data assimilation with the ensemble Kalman filter, Monthly Weather Review, 130, 103-114, 2002.

Richardson, H., Basu, S., and Holtslag, A. A. M.: Improving Stable Boundary-Layer Height Estimation Using a Stability-Dependent Critical Bulk Richardson Number,

Boundary-Layer Meteorology, 148, 93-109, 2013.

Ruiz, J. and Pulido, M.: Parameter Estimation Using Ensemble-Based Data Assimilation in the Presence of Model Error, Monthly Weather Review, 143, 1568-1582, 2015.

Sarwar, G., Simon, H., Bhave, P., and Yarwood, G.: Examining the impact of heterogeneous nitryl chloride production on air quality across the United States, Atmospheric Chemistry and Physics, 12, 6455-6473, 10.5194/acp-12-6455-2012, 2012.

Sasaki, Y.: SOME BASIC FORMALISMS IN NUMERICAL VARIATIONAL ANALYSIS, Monthly Weather Review, 98, 875-&, 1970.

Schneising, O., Buchwitz, M., Burrows, J. P., Bovensmann, H., Bergamaschi, P., and Peters, W.: Three years of greenhouse gas column-averaged dry air mole fractions retrieved from satellite - Part 2: Methane, Atmospheric Chemistry and Physics, 9, 443-465, 2009.

Schwartz, C. S., Liu, Z., Lin, H.-C., and Cetola, J. D.: Assimilating aerosol observations with a "hybrid" variational-ensemble data assimilation system, Journal Of Geophysical Research-Atmospheres, 119, 4043-4069, 10.1002/2013jd020937, 2014.

Sekiyama, T. T., Tanaka, T. Y., Shimizu, A., and Miyoshi, T.: Data assimilation of CALIPSO aerosol observations, Atmospheric Chemistry and Physics, 10, 39-49, 10.5194/acp-10-39-2010, 2010.

Shen, Y., Jiang, F., Feng, S., Zheng, Y., Cai, Z., and Lyu, X.: Impact of weather and emission changes on NO_2 concentrations in China during 2014–2019, Environmental Pollution, 269, 116163, 10.1016/j.envpol.2020.116163, 2021.

Shi, X. and Brasseur, G. P.: The Response in Air Quality to the Reduction of Chinese Economic Activities During the COVID-19 Outbreak, 47, e2020GL088070, 10.1029/2020gl088070, 2020.

Stanevich, I., Jones, D. B. A., Strong, K., Keller, M., Henze, D. K., Parker, R. J., Boesch, H., Wunch, D., Notholt, J., Petri, C., Warneke, T., Sussmann, R., Schneider, M., Hase, F., Kivi, R., Deutscher, N. M., Velazco, V. A., Walker, K. A., and Deng, F.: Characterizing model errors in chemical transport modeling of methane: using GOSAT XCH4 data with weak-constraint four-dimensional variational data assimilation, Atmospheric Chemistry and Physics, 21, 9545-9572, 2021.

Stavrakou, T., Müller, J.-F., Boersma, K. F., De Smedt, I., and van der A, R. J.: Assessing the distribution and growth rates of NOx emission sources by inverting a 10-year record of NO_2 satellite columns, 35, 10.1029/2008gl033521, 2008.

Sun, A. Y., Morris, A., and Mohanty, S.: Comparison of deterministic ensemble Kalman filters for assimilating hydrogeological data, Advances in Water Resources, 32, 280-292, 10.1016/j.advwatres.2008.11.006, 2009.

Takagi, H., Saeki, T., Oda, T., Saito, M., Valsala, V., Belikov, D., Saito, R., Yoshida, Y., Morino, I., Uchino, O., Andres, R. J., Yokota, T., and Maksyutov, S.: On the Benefit of GOSAT Observations to the Estimation of Regional CO_2 Fluxes, SOLA, 7, 161-164, 10.2151/sola.2011-041, 2011.

Tang, X., Zhu, J., Wang, Z. F., and Gbaguidi, A.: Improvement of ozone forecast over Beijing based on ensemble Kalman filter with simultaneous adjustment of initial conditions and emissions, Atmospheric Chemistry And Physics, 11, 12901-12916, 10.5194/acp-11-12901-2011, 2011.

Tang, X., Zhu, J., Wang, Z. F., Wang, M., Gbaguidi, A., Li, J., Shao, M., Tang, G. Q., and Ji, D. S.:

Inversion of CO emissions over Beijing and its surrounding areas with ensemble Kalman filter, Atmospheric Environment, 81, 676-686, 10.1016/j.atmosenv.2013.08.051, 2013.

Wang, C., Lei, L., Tan, Z.-M., and Chu, K.: Adaptive Localization for Tropical Cyclones With Satellite Radiances in an Ensemble Kalman Filter, Frontiers in Earth Science, 8, 10.3389/feart.2020.00039, 2020.

Wang, H., Jiang, F., Wang, J., Ju, W., and Chen, J. M.: Terrestrial ecosystem carbon flux estimated using GOSAT and OCO-2 XCO2 retrievals, Atmospheric Chemistry and Physics, 19, 12067-12082, 2019a.

Wang, N., Lyu, X., Deng, X., Huang, X., Jiang, F., and Ding, A.: Aggravating O3 pollution due to NOx emission control in eastern China, Science of The Total Environment, 677, 732-744, 2019b.

Wang, Y. H., Hu, B., Ji, D. S., Liu, Z. R., Tang, G. Q., Xin, J. Y., Zhang, H. X., Song, T., Wang, L. L., Gao, W. K., Wang, X. K., and Wang, Y. S.: Ozone weekend effects in the Beijing-Tianjin-Hebei metropolitan area, China, Atmospheric Chemistry and Physics, 14, 2419-2429, 2014.

Wang, Z., Li, Y., Dong, X., Sun, R., Sun, N., and Pan, L.: Analysis on weekend effect of air pollutants in urban atmosphere of Beijing, Journal of University of Chinese Academy of Sciences, 32, 843-850, 2015.

Wang, Z., Wang, W., Tham, Y.J., Li, Q., Wang, H., Wen, L., Wang, X., Wang, T., 2017. Fast heterogeneous N2O5 uptake and ClNO2 production in power plant and industrial plumes observed in the nocturnal residual layer over the North China Plain. Atmospheric Chemistry and Physics 17, 12361-12378.

Wecht, K. J., Jacob, D. J., Sulprizio, M. P., Santoni, G. W., Wofsy, S. C., Parker, R., Boesch, H., and Worden, J.: Spatially resolving methane emissions in California: constraints from the CalNex aircraft campaign and from present (GOSAT, TES) and future (TROPOMI, geostationary) satellite observations, Atmospheric Chemistry and Physics, 14, 8173-8184, 2014.

Wu, H., Tang, X., Wang, Z., Wu, L., Li, J., Wang, W., Yang, W., and Zhu, J.: High-spatiotemporal-resolution inverse estimation of CO and NOx emission reductions during emission control periods with a modified ensemble Kalman filter, Atmospheric Environment, 236, 10.1016/j.atmosenv.2020.117631, 2020.

Wu, W. S., Purser, R. J., and Parrish, D. F.: Three-dimensional variational analysis with spatially inhomogeneous covariances, Monthly Weather Review, 130, 2905-2916, 10.1175/1520-0493(2002)130<2905:tdvaws>2.0.co;2, 2002.

Yang, W., Li, J., Wang, W., Li, J., Ge, M., Sun, Y., Chen, X., Ge, B., Tong, S., Wang, Q., and Wang, Z.: Investigating secondary organic aerosol formation pathways in China during 2014, Atmospheric Environment, 213, 133-147, 2019.

Zhang, F., Weng, Y., Sippel, J. A., Meng, Z., and Bishop, C. H.: Cloud-Resolving Hurricane Initialization and Prediction through Assimilation of Doppler Radar Observations with an Ensemble Kalman Filter, Monthly Weather Review, 137, 2105-2125, 10.1175/2009mwr2645.1, 2009a.

Zhang, L., Chen, Y., Zhao, Y., Henze, D. K., Zhu, L., Song, Y., Paulot, F., Liu, X., Pan, Y., Lin, Y., and Huang, B.: Agricultural ammonia emissions in China: reconciling bottom-up and top-down estimates, Atmospheric Chemistry and Physics, 18, 339-355, 2018.

Zhang, Q., Streets, D. G., Carmichael, G. R., He, K. B., Huo, H., Kannari, A., Klimont, Z., Park, I.

S., Reddy, S., Fu, J. S., Chen, D., Duan, L., Lei, Y., Wang, L. T., and Yao, Z. L.: Asian emissions in 2006 for the NASA INTEX-B mission, Atmospheric Chemistry and Physics, 9, 5131-5153, 10.5194/acp-9-5131-2009, 2009b.

Zhang, S., Zheng, X., Chen, J. M., Chen, Z., Dan, B., Yi, X., Wang, L., and Wu, G.: A global carbon assimilation system using a modified ensemble Kalman filter, Geosci. Model Dev., 8, 805-816, 10.5194/gmd-8-805-2015, 2015.

Zhang, X., Liu, J., Han, H., Zhang, Y., Jiang, Z., Wang, H., Meng, L., Li, Y. C., and Liu, Y.: Satellite-Observed Variations and Trends in Carbon Monoxide over Asia and Their Sensitivities to Biomass Burning, Remote Sensing, 12, 10.3390/rs12050830, 2020.

Zheng, B., Tong, D., Li, M., Liu, F., Hong, C., Geng, G., Li, H., Li, X., Peng, L., Qi, J., Yan, L., Zhang, Y., Zhao, H., Zheng, Y., He, K., and Zhang, Q.: Trends in China's anthropogenic emissions since 2010 as the consequence of clean air actions, Atmospheric Chemistry And Physics, 18, 14095-14111, 10.5194/acp-18-14095-2018, 2018.